
Supplementary information

Topographic organization of the human subcortex unveiled with functional connectivity gradients

In the format provided by the
authors and unedited

Topographic organization of the human subcortex unveiled with functional connectivity gradients

Ye Tian^{1*}, Daniel S. Margulies², Michael Breakspear³, Andrew Zalesky^{1,4*}

1. Melbourne Neuropsychiatry Centre, Department of Psychiatry, The University of Melbourne, Parkville, VIC, Australia
2. Centre National de la Recherche Scientifique (CNRS) UMR 8002, Integrative Neuroscience & Cognition Center, Université de Paris, France
3. Discipline of Psychiatry, Faculty of Health and Medicine, and School of Psychology, Faculty of Science, University of Newcastle, NSW, Australia
4. Department of Biomedical Engineering, Melbourne School of Engineering, The University of Melbourne, Parkville, VIC, Australia

*Correspondence: Dr Ye Tian ye.tian2@unimelb.edu.au

Dr Andrew Zalesky azalesky@unimelb.edu.au

Supplementary Information

Table of Contents

Supplementary Figures

- Figure 1. Mapping of Gradient II and III.*
- Figure 2. Variance explained by successive gradients.*
- Figure 3. Impact of left-right symmetrization on gradient magnitude images.*
- Figure 4. Spatial variation in primary MRI signal properties in the subcortex.*
- Figure 5. Testing whether gradient magnitude peaks are large enough to warrant boundary delineation.*
- Figure 6. Criteria used to justify boundary delineation.*
- Figure 7. Organization of connectivity gradients in the human subcortex.*
- Figure 8. Schematic of fMRI data preprocessing and boundary delineation.*
- Figure 9. Spatial correspondence between the new atlas and histological parcellations of thalamus and hippocampus.*
- Figure 10. Projection of gradients within specific subcortical nuclei onto the cortical surface.*
- Figure 11. Schematic of parcellation homogeneity estimation.*
- Figure 12. Parcellation homogeneity of the new and existing subcortical parcellation atlases.*
- Figure 13. Parcellation homogeneity estimated in an independent validation dataset.*
- Figure 14. Quantifying the extent to which task-evoked activity is circumscribed to regions comprising the atlas for Scale I-IV.*
- Figure 15. 3 Tesla and 7 Tesla subcortex parcellation at Scale IV.*
- Figure 16. Quantitative comparison between 3 Tesla and 7 Tesla atlas across parcellation scales.*
- Figure 17. Schematic of methodology for parcellation personalization.*
- Figure 18. Within-subject variation in Dice coefficient across subcortical regions.*
- Figure 19. Variation in subcortical connectivity gradients between rest and task-evoked conditions.*
- Figure 20. Linking canonical cortical networks based on their functional connectivity with subcortical regions.*
- Figure 21. Behavioral dimensions.*
- Figure 22. Association between subcortical functional connectivity and the behavioral dimension characterizing tobacco use reproduced using functional MRI from a second session.*
- Figure 23. Model selection with Kolmogorov-Smirnov (KS) test.*
- Figure 24. Determining the optimal number of independent components.*

Supplementary Tables

- Table 1. Basic demographic characteristics and acquisition details.*
- Table 2. Nomenclature for 3T parcellation hierarchy.*
- Table 3. Comparison parcellation atlases of the human subcortex and specific subcortical nuclei.*
- Table 4. List of 109 selected behavioral items.*
- Table 5. NIFTI and CIFTI file names for 3T and 7T atlas.*

Supplementary References

Supplementary Figures

All anatomical images and renderings are shown in Montreal Neurological Institute (MNI, 6th generation) anatomical reference space. Slice location of images is indicated in MNI coordinates (millimeters). Background images are derived from the MNI152 standard-space T1-weighted average reference image. For visualization of the 7T atlas, the reference image was resliced to the resolution of the 7T functional MRI data.

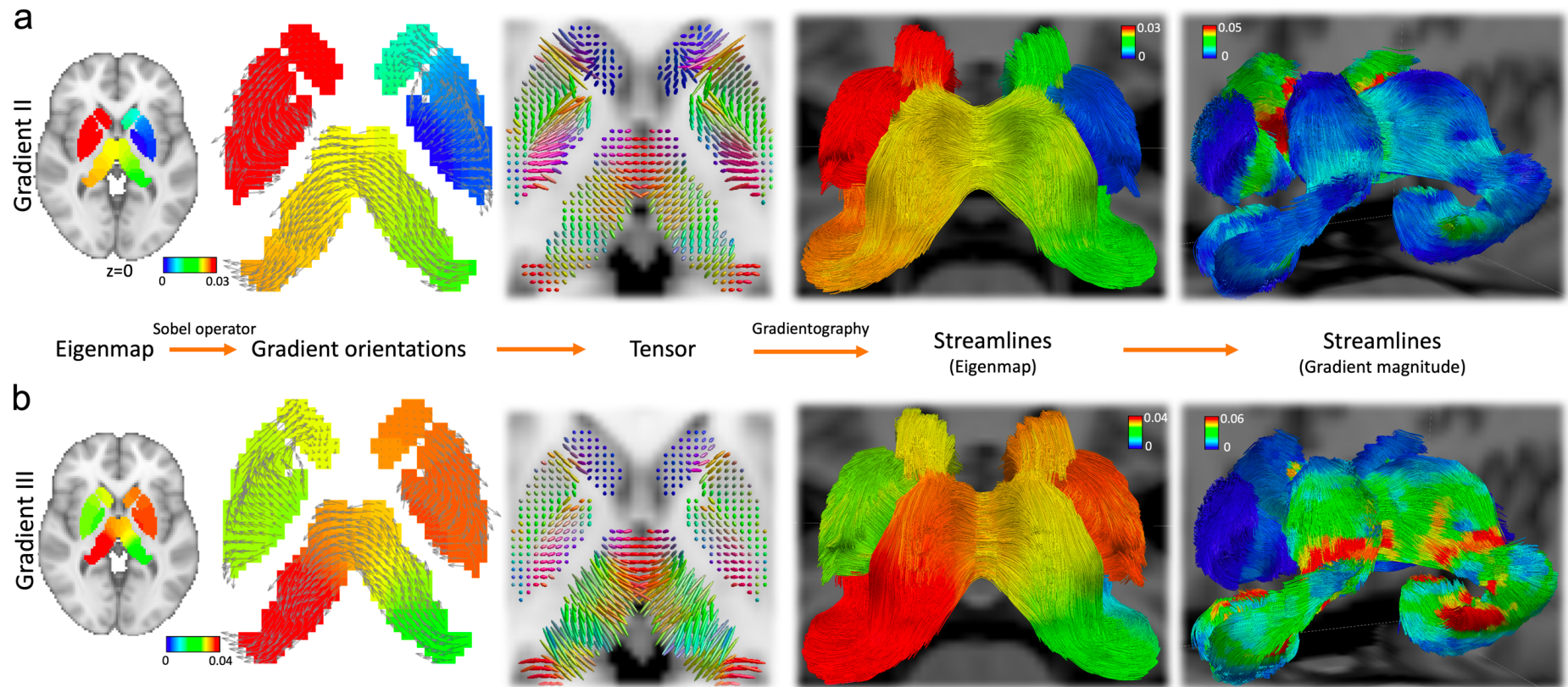


Figure 1. Mapping of Gradient II and III. Group-consensus eigenmaps, tensors and gradientography for Gradient II (a) and Gradient III (b). Gradients were mapped to subcortical voxels to enable anatomical visualization. Eigenmaps for each gradient are shown as axial slices, with a reference structural MRI image used as the background. The Sobel operator was used to estimate the local gradient direction and magnitude for each subcortical voxel. The arrows shown point in the direction of the estimated gradients. Arrow lengths are commensurate with gradient magnitude. Tensors were fitted to the gradient field. Tensors are colored according to gradient direction (blue: superior-inferior, red: left-right, green: posterior-anterior). Long cigar-shaped tensors indicate large gradient magnitudes. Streamlines were propagated through the tensor field using tools for diffusion MRI tractography. Streamlines are colored according to eigenmaps (second from right) and gradient magnitude (rightmost). Local maxima in the gradient magnitude are evident within circumscribed bands along streamlines, indicating putative functional boundaries. While Gradient I characterized an ipsilateral

organizational axis with extremes located at amygdala and globus pallidus (see Figure 1b), Gradient II and III maximally differentiated contralateral regions in dorsal (bilateral globus pallidus) and ventral (bilateral amygdala), respectively. Of note, the anterior-posterior or rostrocaudal axis explains much of the spatial variation in cortical microstructure, which is evident in a broad range of the mammalian species, including rodents, marsupials and primates¹⁻⁴. This rostrocaudal organization also aligns with the spatial gradients in neurodevelopment^{5,6}.

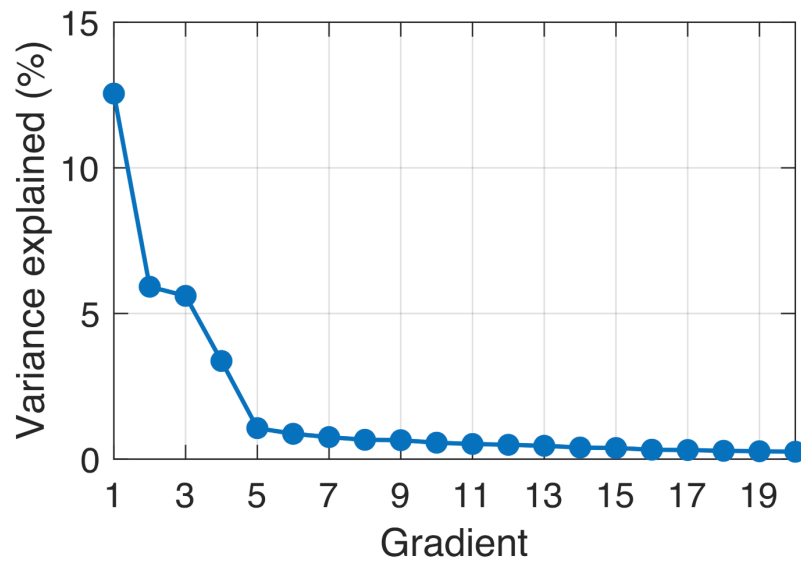


Figure 2. Variance explained by successive gradients. Variance explained in subcortical functional connectivity by successive gradients (Laplacian eigenvectors) shown as a function of gradient index, ordered from smallest to largest eigenvalue. The eigenvector associated with the second smallest eigenvalue is labelled Gradient I, while the eigenvector with the third smallest eigenvalue is labelled Gradient II, and so on. The variance explained by the first 20 eigenvectors is shown. The variance explained by Gradient IV and beyond falls below 5%, and thus only Gradients I-III are analyzed in this study.

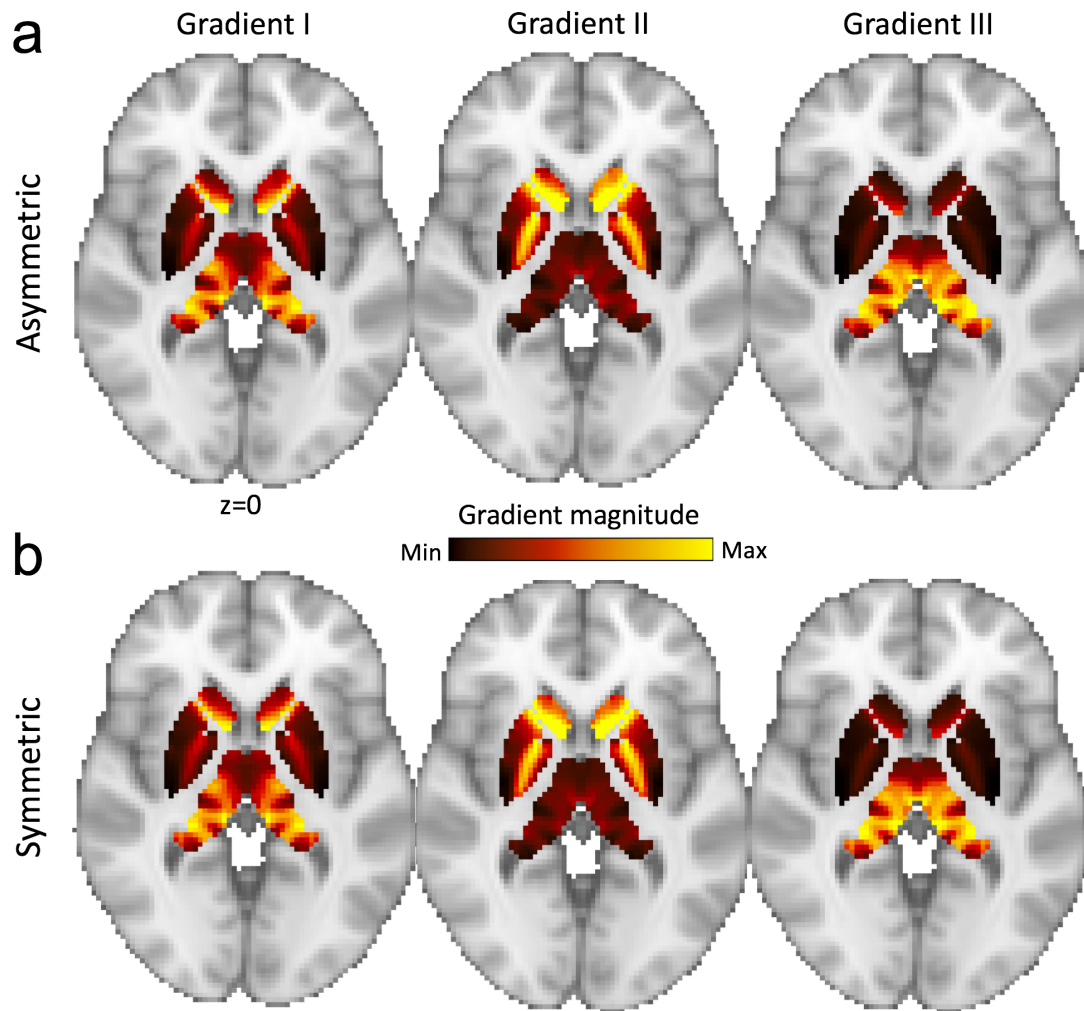


Figure 3. Impact of left-right symmetrization on gradient magnitude images. Left-right symmetrization was performed to enhance the signal-to-noise ratio. **a**, Gradient magnitude images for Gradient I-III without left-right symmetrization. Images show a large degree of left-right symmetry, even without explicit symmetrization. **b**, Left-to-right symmetrized gradient magnitude images. Images are shown as axial slices, with a reference structural MRI image used as the background. The same axial slice is used for all images.

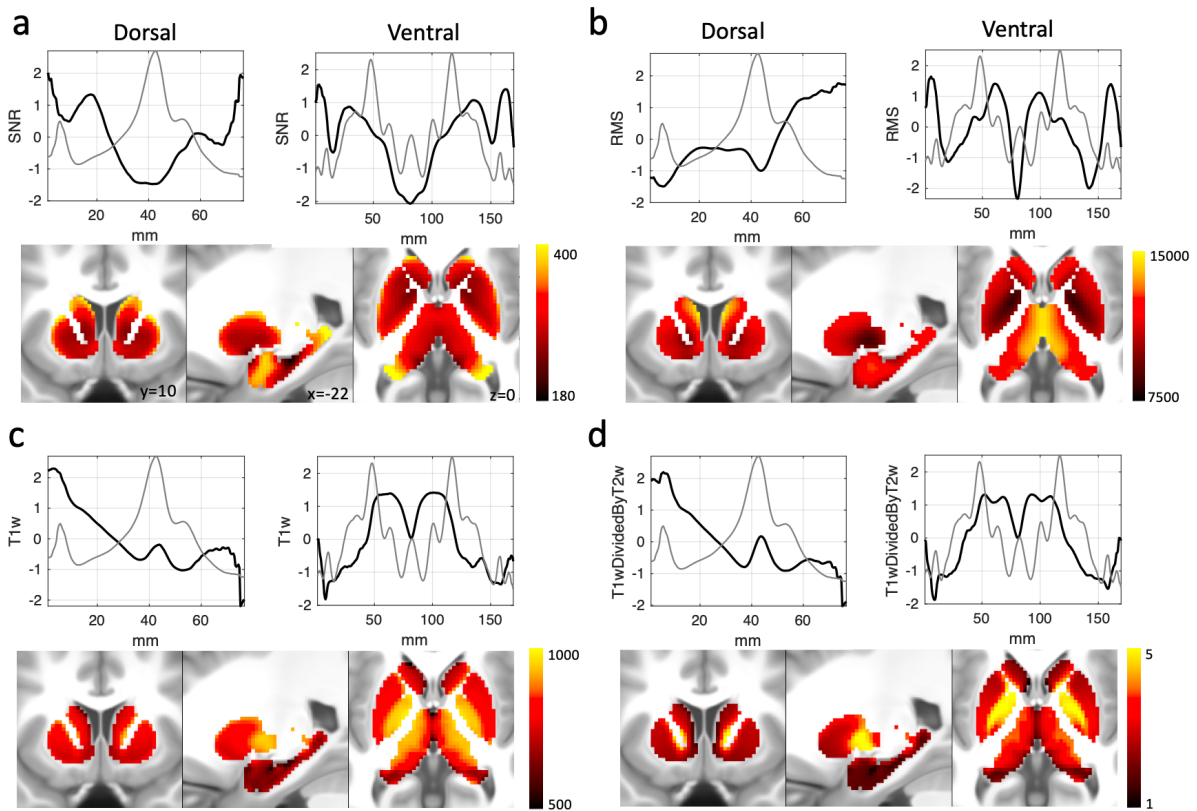


Figure 4. Spatial variation in primary MRI signal properties in the subcortex. **a**, Signal-to-noise ratio (SNR) was computed for each subcortical voxel by averaging the signal intensity across all time frames in each run of the preprocessed fMRI data and normalizing by the standard deviation over time⁷. SNR was averaged across runs for each individual and then averaged across individuals (REST1, n=1080) to yield a group-consensus subcortical SNR map. **b**, Blood-oxygenation level dependent (BOLD) signal magnitude was computed for each subcortical voxel by calculating the root mean squared (RMS) of the signal intensity over time. RMS was then averaged across individuals, yielding a group-consensus subcortical BOLD signal magnitude map. **c**, Group-averaged (S1200) T1-weighted contrast in the subcortex resliced to 2mm isotropic voxel resolution. **d**, Group-averaged (S1200) T1/T2-weighted contrast resliced to 2mm isotropic voxel resolution. The spatial correlation between each of the four group-consensus signal maps and the connectivity gradient magnitude map (Figure 6a) was quantified by the Spearman correlation coefficient (SNR: $r=-0.21$; RMS: $r=0.42$; T1-weighted: $r=0.02$; T1/T2-weighted: $r=0.02$). The four group-consensus signal maps were then projected onto the previously mapped streamlines (Figure 2), yielding dorsal and ventral diversity curves (black) for each of the four signal maps. The diversity curves for each of these four measures do not recapitulate peaks in the gradient magnitude images (light gray), suggesting that spatial variation in structural factors and SNR does not appear to confound the computation of functional connectivity gradients.

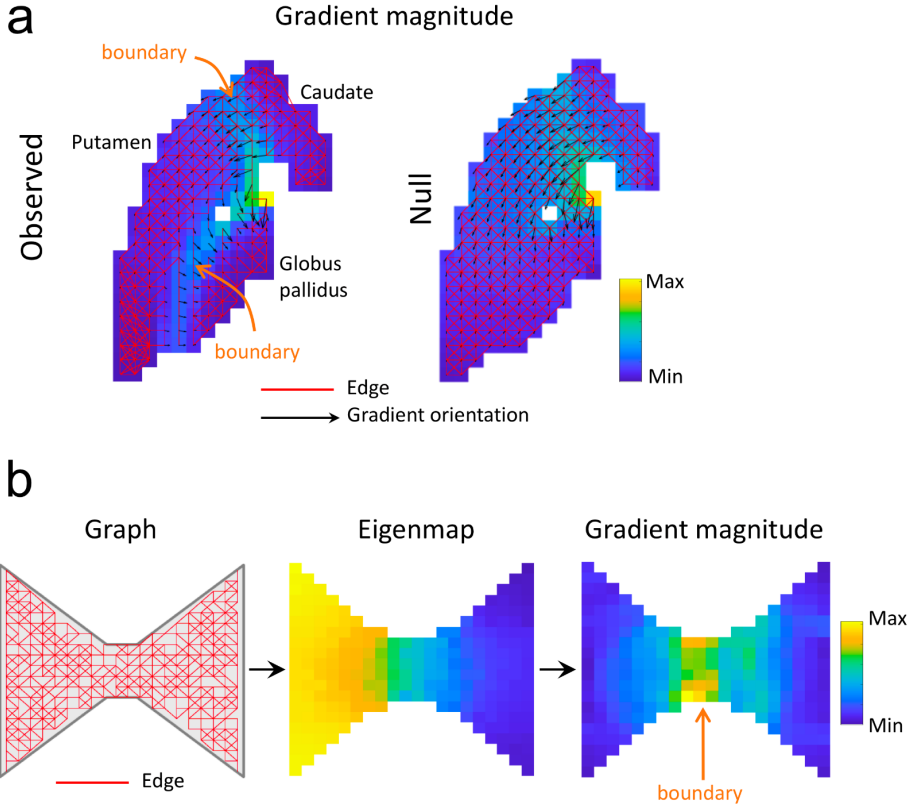


Figure 5. Testing whether gradient magnitude peaks are large enough to warrant boundary delineation. Null data was generated to test the null hypothesis that a gradient magnitude peak was due to chance, the geometry of the subcortex and/or other confounds. The alternative hypothesis was that the peak demarcated a discrete boundary in functional connectivity topography. **a**, Graph defined by the sparse adjacency matrix W computed from empirical fMRI data (observed data) is compared to one rewired graph generated from the null data (\bar{W}_1). Nodes in the graph correspond to subcortical voxels. Edges (solid red lines) are drawn between voxels that share similar functional connectivity profiles. Axial slices from the gradient magnitude images are shown in the background of each graph. It should be noted that very few edges in the graph for W (observed data) traverse the functional boundary between globus pallidus and putamen (indicated by orange arrows), whereas the graph for \bar{W}_1 (null data) comprises a number of rewired edges that cross this boundary. Therefore, unlike the observed data, a peak in the gradient magnitude image between the globus pallidus and putamen is absent in the null data, suggesting that the null hypothesis can be rejected for this particular boundary. Indeed, this was confirmed by generating 100 rewired graphs ($\bar{W}_1, \bar{W}_2, \dots, \bar{W}_{100}$) and showing that the proportion of rewired graphs with peaks at this location that exceeded the peak in W did not exceed 5%. **b**, Hypothetical example demonstrating how the effect of geometry alone can intrinsically lead to delineation of spurious boundaries. Edges (solid red lines) were randomly placed between pairs of neighboring pixels residing within a hypothetical bow-tie shaped object (left). Random placement of edges between neighboring pixels is consistent with the null hypothesis of a uniform spatial gradient (i.e. rate of change in gradient is homogenous across the extent of the bow tie). The Laplacian eigenmap (center) and the eigenmap's gradient magnitude (right) is shown for the graph (left). Note the peak in the gradient magnitude image that is located at the knot of the bow tie (indicated by the orange arrow), providing evidence for a putative boundary, despite the null hypothesis being true by design. The

gradient magnitude peak is exclusively due to the geometric constriction owing to the knot. Edges are more likely to be placed within the ends of the bow tie, rather than within the knot, because the ends occupy a comparably larger area. This hypothetical example demonstrates the importance of accounting for geometry when generating null data to test whether gradient magnitude peaks are sufficiently large to warrant boundary delineation. Without accounting for the effect of geometry, specious boundaries could potentially be delineated due to the convoluted geometry of the subcortex.

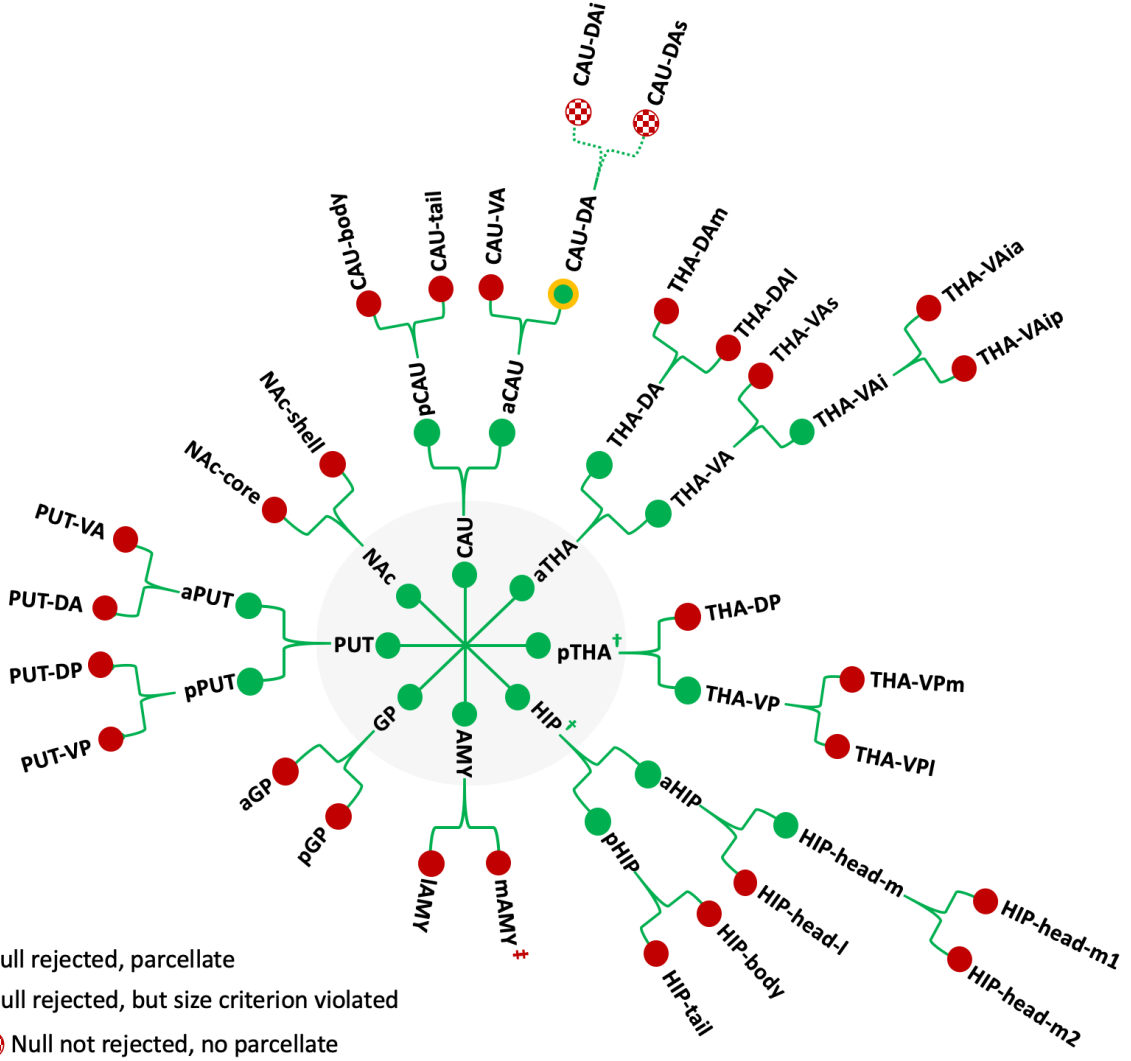


Figure 6. Criteria used to justify boundary delineation. Model selection and null hypothesis testing was used to determine whether gradient magnitude peaks were sufficiently large to warrant boundary delineation. This process was repeated recursively for each new region delineated, unveiling a multiscale parcellation architecture. The parcellation hierarchy is visualized in the form of a circular tree. The central node represents the entire subcortex and other nodes represent distinct regions. Regions are arranged within four concentric circles, where the innermost circle (gray) is the first level (Scale I). Nodes are colored according to criterion used to justify further boundary delineation within the region or to terminate the branch of the hierarchy. For the vast majority of regions, null hypothesis testing determined whether or not a boundary was delineated. However, additional criteria were used for three regions (see Methods). Green: null rejected, parcellate; green with yellow circle: null rejected, but size criterion violated and resulting parcels considered too small to delineate (size criterion); red: null not rejected, no parcellate. \dagger : prior knowledge criterion; \ddagger : inter-hemispheric homologue criterion. If the size criterion were to be relaxed, the dorsoanterior caudate (CAU-DA) would be subdivided into inferior and superior component.

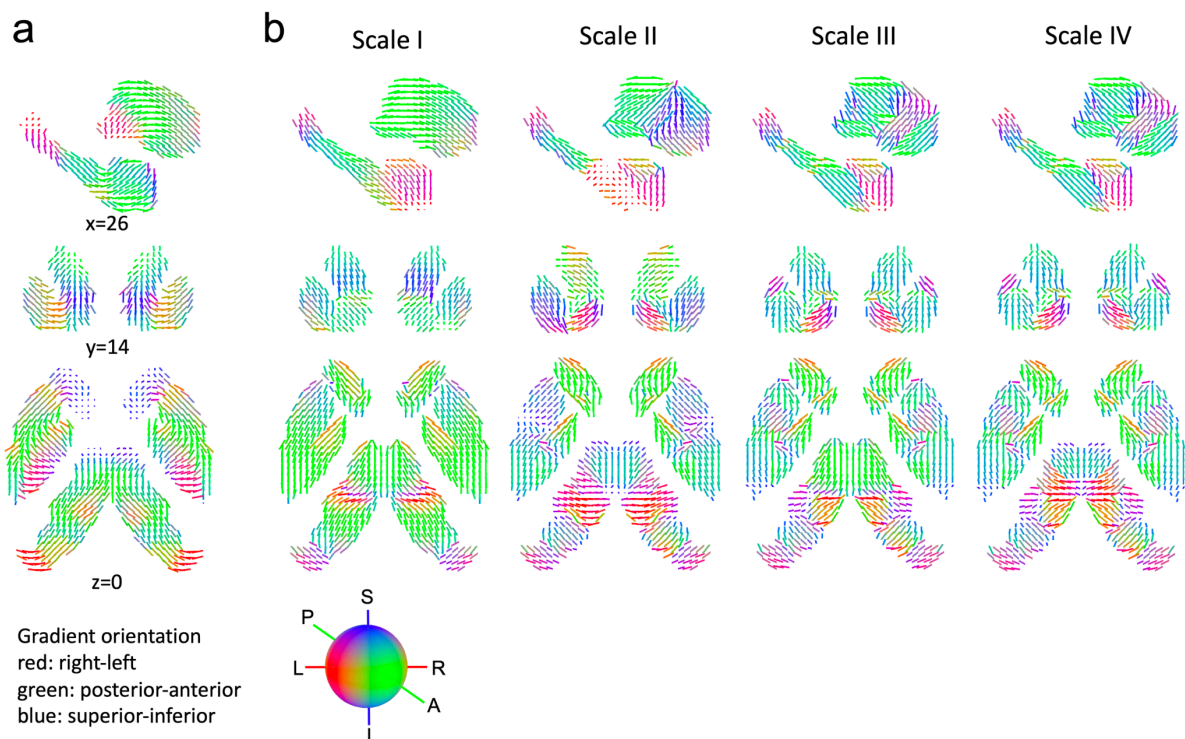


Figure 7. Organization of connectivity gradients in the human subcortex. **a**, The quiver lines represent gradient directions for each voxel. Each quiver is colored according to gradient direction (red: left-right, green: posterior-anterior, blue: superior-inferior) and scaled to unit length. **b**, Gradients are hierarchically organized along the parcellation hierarchy. Local gradient direction in each subcortical voxel was estimated within each region at each atlas scale (Scale I–IV).

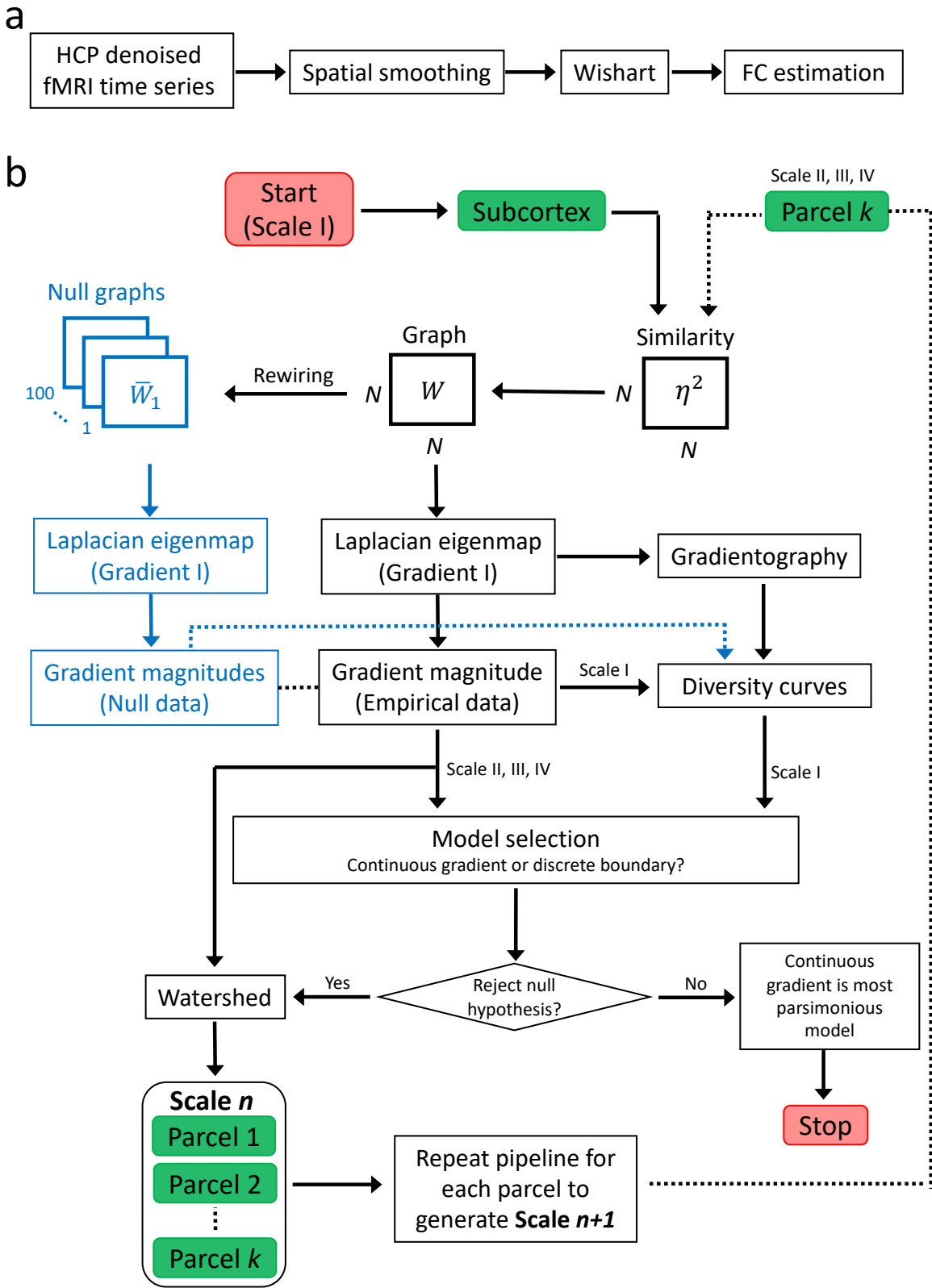


Figure 8. Schematic of fMRI data preprocessing and boundary delineation. **a**, The minimally preprocessed and denoised (ICA+FIX) fMRI data were sourced from the HCP. The preprocessed data were spatially smoothed and then adjusted using a recently developed Wishart filter^{8, 9} to further improve the signal-to-noise ratio. The 3T images were smoothed with a Gaussian smoothing kernel of 6mm FWHM (full width at half maximum), whereas

4mm FWHM was used for the 7T images. Using the preprocessed fMRI data, functional connectivity (FC) was then measured between each subcortical voxel and all other cortical and subcortical voxels, as shown in Figure 1a. A similarity matrix was computed for each individual to quantify the extent of similarity in the functional connectivity profiles of all pairs of subcortical voxels. **b**, Boundary delineation pipeline. The subcortex was recursively parcellated into increasingly fine functional subdivisions, until the null hypothesis of a single, continuous region with no discrete boundaries could no longer be rejected, yielding a multiscale characterization of subcortical architecture. Rejection of the null hypothesis indicated that further subdivision of a region was warranted, leading to delineation of a finer scale. Model selection refers to the decision of whether to delineate a discrete boundary or represent spatial variation in functional connectivity as a gradual continuum. The arrow connecting the end of the pipeline to the beginning indicates the recursive nature of the pipeline, where each new recursion designates a finer parcellation scale. The flowchart shows that the entire pipeline (i.e. gradient mapping, null data and model selection) is performed separately for each newly delineated region, until the null hypothesis cannot be rejected. Model selection was performed differently for Scale I compared to the finer scales. For Scale I, where multiple candidate boundaries were observed, local peaks in the gradient magnitude in the diversity curves generated from the empirical data were benchmarked against the diversity curves generated with the null model (blue blocks). Model selection was performed to test whether the peak magnitude was sufficiently large (i.e. exceeded the null distribution) to warrant boundary demarcation. Next, the watershed transform algorithm was used to segment subcortical voxels into contiguous parcels. For finer scales (Scale >1), where regions were small and usually comprised a single candidate boundary, the Kolmogorov-Smirnov (KS) test was used to assess the null hypothesis of equality in the distribution across voxels between the observed gradient magnitudes and the null gradient magnitudes. The null hypothesis was rejected if the tail of the distribution of the gradient magnitude was longer in the empirical data. Other criteria that informed the decision of boundary delineation include: i) minimum size criterion to avoid excessively small regions; ii) prior anatomical knowledge; and, iii) presence of inter-hemispheric homologues. Similarly, the watershed transform algorithm was used to generate subcortical parcels. See Figure 1 for detailed gradient mapping and gradientography pipelines.

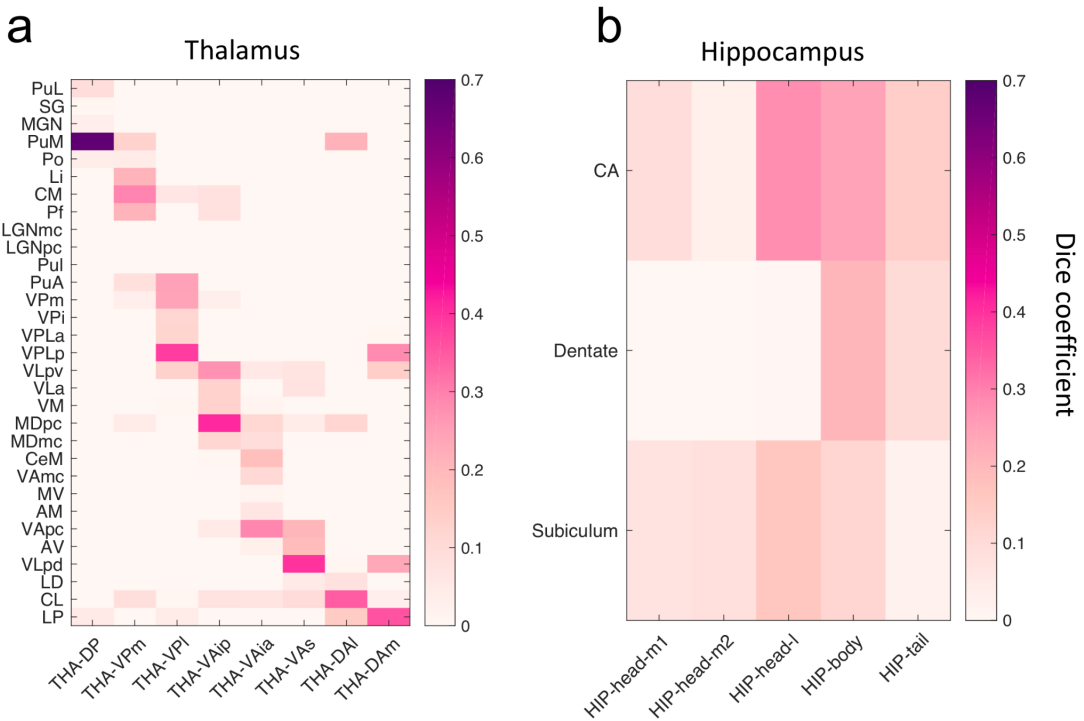


Figure 9. Spatial correspondence between the new atlas and histological parcellations of thalamus and hippocampus. **a**, Dice coefficient is shown between each thalamic anatomical nucleus comprising an existing histological atlas¹⁰ (vertical axis) and each functional thalamic region delineated at Scale IV (horizontal axis). Despite the mismatch in parcellation resolution, several thalamic regions comprising the new atlas can be uniquely mapped to one, or a cluster, of histologically delineated nuclei. For example, THA-DP uniquely maps to PuM, whereas THA-VPM maps to Pf, CM and Li. The spatial correspondence is moderate to good (Dice coefficient: 0.3-0.7), although several histological nuclei cannot be uniquely assigned to a region in the new atlas (e.g. SG). Abbreviations of anatomical nuclei: PuL, inferior pulvinar; SG, suprageniculate nucleus; MGN, medial geniculate nucleus; PuM, medial pulvinar; Po, posterior pulvinar; Li, limitans nucleus; CM, centre median nucleus; Pf, parafascicular nucleus; LGNmc, lateral geniculate nucleus (manocellular part); LGNpc, lateral geniculate nucleus (parvocellular part); PuL, lateral pulvinar; PuA, anterior pulvinar; VPm, ventral posterior medial nucleus; VPi, ventral posterior inferior nucleus; VPLa, ventral posterior lateral nucleus (anterior part); VPLp, ventral posterior lateral nucleus (anterior part); VLpv, ventral lateral posterior nucleus (ventral part); VLa, ventral lateral anterior nucleus; VM, ventral medial nucleus; MDpc, mediodorsal nucleus (parvocellular part); MDmc, mediodorsal nucleus (manocellular part); CeM, central medial nucleus; VAmc, ventral anterior nucleus (magnocellular part); MV, medioventral nucleus; AM, anterior medial nucleus; VApc, ventral anterior nucleus (parvocellular part); AV, anterior ventral nucleus; VLpd, ventral lateral posterior nucleus (anterior part); LD, lateral dorsal nucleus; CL, central lateral nucleus; LP, lateral posterior nucleus. **b**, Dice coefficient is shown between each hippocampal subfield^{11, 12} (vertical axis) and each functional hippocampal region delineated at Scale IV (horizontal axis). Unlike the thalamus, spatial correspondence between the histologically defined hippocampal subfields and the new atlas is relatively poor. This is because the subfields are delineated approximately parallel to the longitudinal hippocampal axis, whereas hippocampus is parcellated perpendicular to this axis in the new atlas. CA, cornu ammonis subfield. Dentate, dentate gyrus.

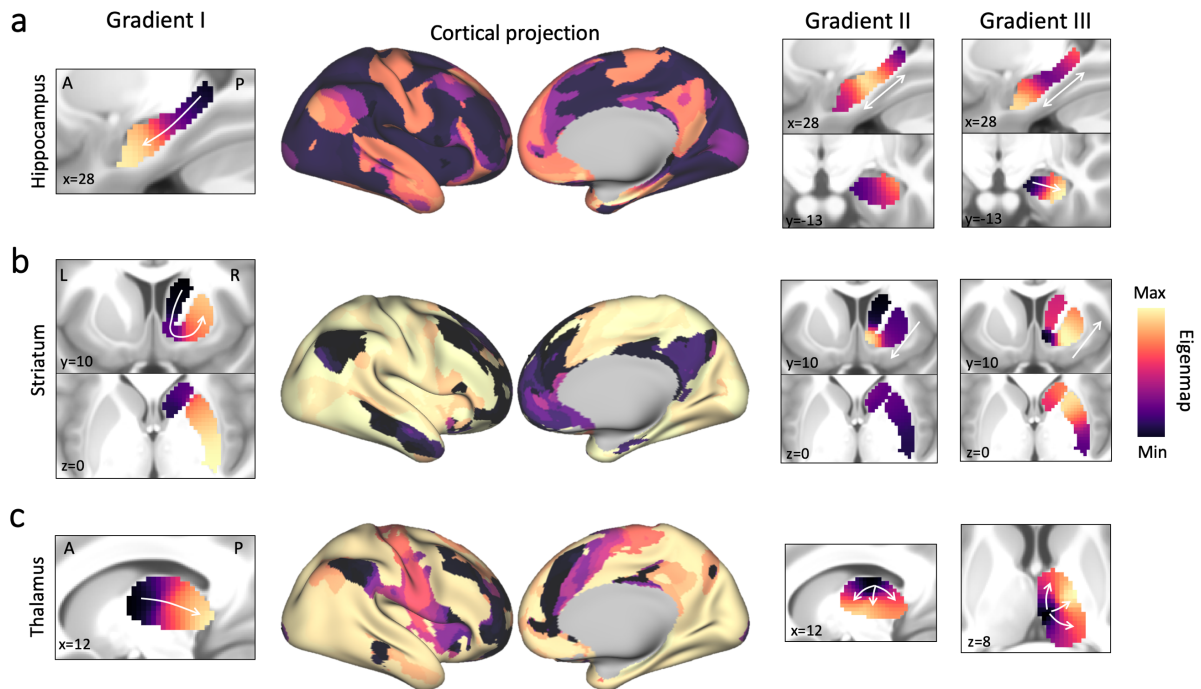


Figure 10. Projection of gradients within specific subcortical nuclei onto the cortical surface. Connectivity gradients within hippocampus (a) striatum (b), and thalamus (c) are shown as projections on the cortical surface for Gradient I. Eigenmaps for Gradients II and III are shown in anatomical space. **a**, Cortical surface projections show that progressively more anterior areas of hippocampus project to progressively more ventromedial parts of the frontal and cingulate cortices. **b**, The dominant striatal gradient separates putamen, NAc and caudate, with NAc and caudate differentially projecting to association networks (i.e. default mode¹³ and frontoparietal network¹⁴) along a ventromedial-to-dorsolateral gradient, and putamen widely projects to other parts of the brain. In contrast, the second and third striatal gradients, are organized along a dorsal-to-ventral axis¹⁵⁻¹⁷. **c**, The anterior thalamus is primarily connected to dorsoanterior cingulate, dorsolateral prefrontal, medial superior frontal and anterior insular cortices, which together form the cingulo-opercular network^{18, 19}. In contrast, the middle-to-posterior thalamus is widely connected to unimodal and multimodal areas, including somatosensory, motor, premotor, visual and auditory cortices, as well as orbital frontal cortex. Gradient I (eigenmap) was projected onto the cortical surface by coloring cortical vertices according to the subcortical voxel with which they were most strongly connected. White arrows indicate principal gradient directions. Functional connectivity between each subcortical voxel and cortical vertex was computed using the preprocessed dense connectome matrix (S1200 release) from the HCP, where the functional connectivity between all pairs of grayordinates (subcortical voxels and cortical vertices) was averaged across 812 individuals and across four runs.

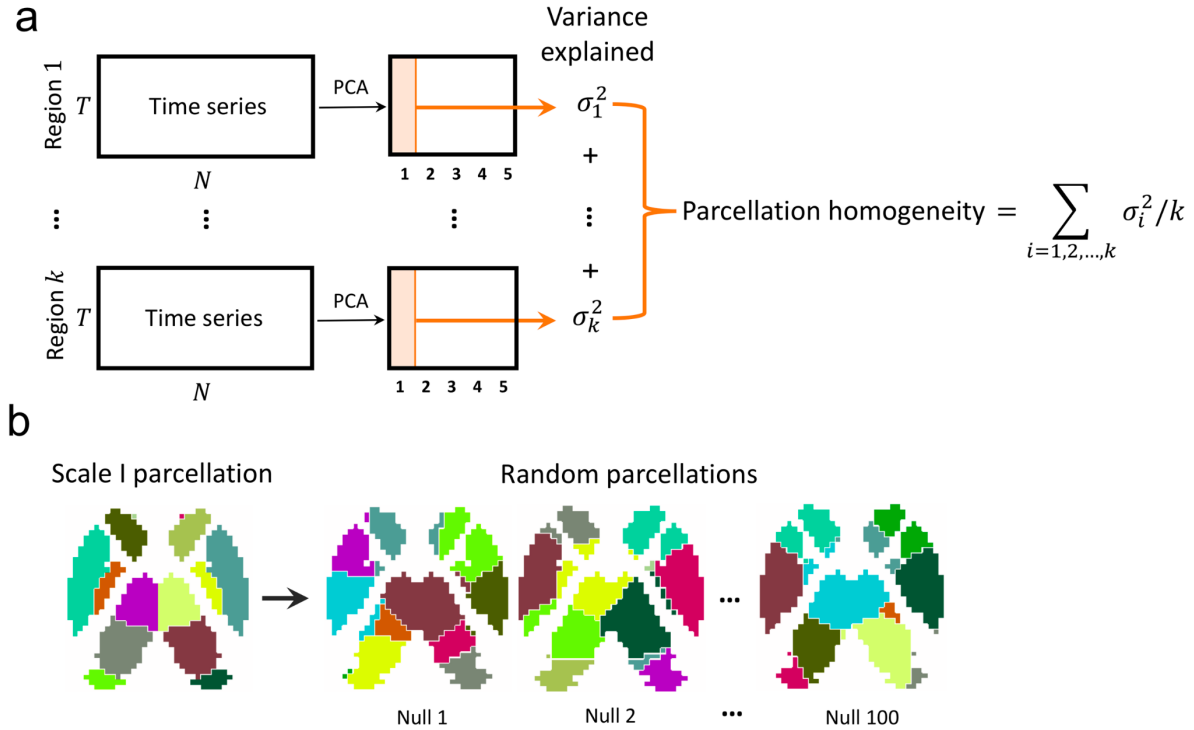


Figure 11. Schematic of parcellation homogeneity estimation. **a**, Schematic and formula representing the computation of parcellation homogeneity. Functional MRI time series for each voxel in a given region were concatenated, yielding a matrix of dimension $N \times T$, where N and T denote the number of voxels comprising the region and the number of time frames, respectively. Following previous work²⁰, principal component analysis (PCA) was applied to this matrix and the variance explained by the first principal component was estimated and referred to as regional homogeneity. The regional homogeneity was computed for each region and for each individual separately. For each individual, regional homogeneity was then averaged across all regions, yielding an overall estimate of parcellation homogeneity. **b**, Images show anatomical visualizations of the Scale I atlas (leftmost) and three instantiations of randomized versions of the atlas (right images). The random parcellations comprise an identical number of regions and comparable distribution of region sizes.

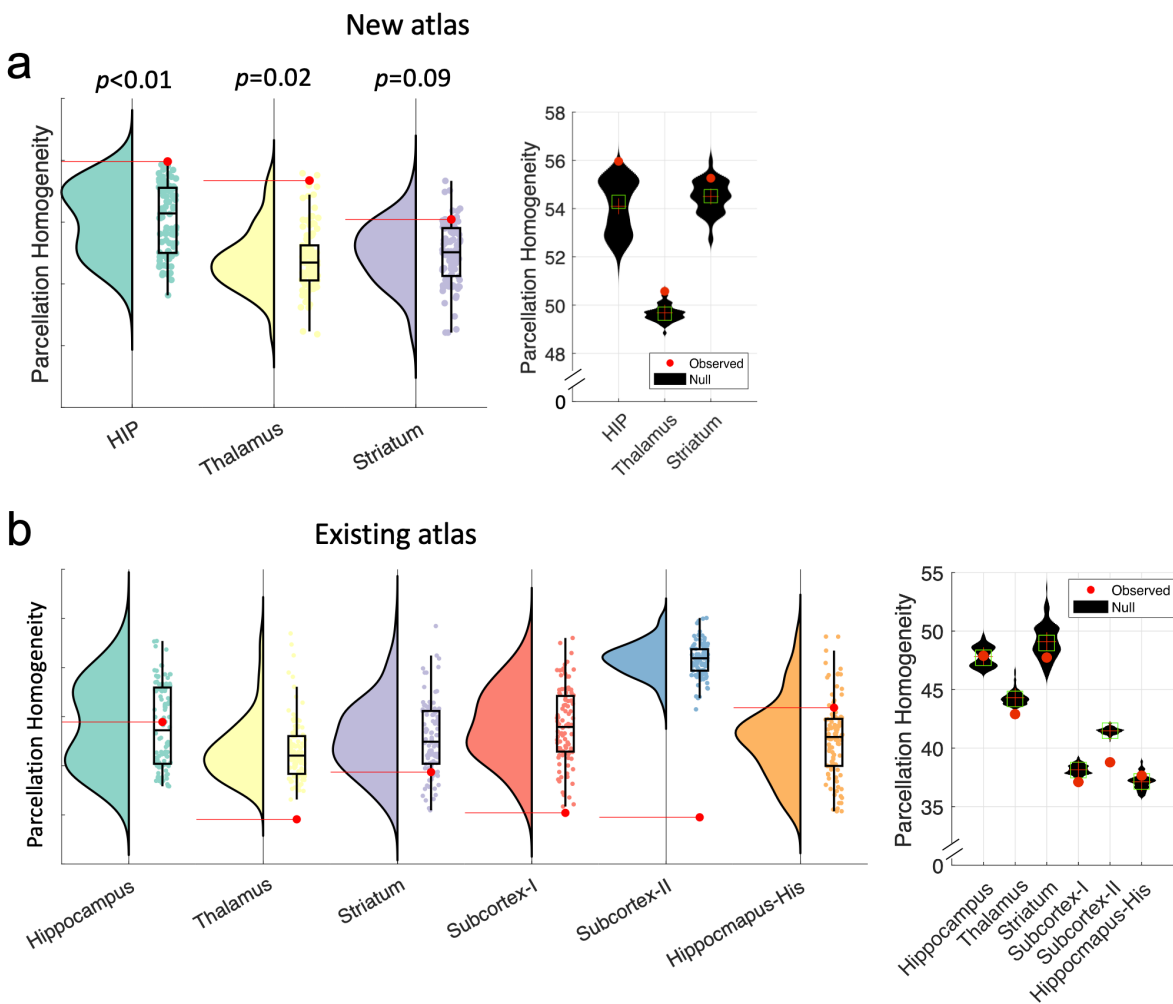


Figure 12. Parcellation homogeneity of the new and existing subcortical parcellation atlases. **a**, Parcellation homogeneity of the new atlas within the hippocampus (HIP), thalamus and striatum were benchmarked to random parcellations comprising an identical number of regions and a comparable distribution of region sizes. The p-value shown for each atlas is the proportion of random parcellations ($n=100$) comprising the ensemble with equal or greater homogeneity than the observed parcellation (one-sided). **b**, Parcellation homogeneity of five existing atlases was benchmarked to random parcellations comprising an identical number of regions and a comparable distribution of region sizes. Violin plots show the distribution of parcellation homogeneity measured within ensembles of 100 such random parcellations. Red dots and horizontal red lines indicate the observed parcellation homogeneity values. Bottom and top edges of the boxes indicate 25th and 75th percentiles of the distribution, respectively. The central mark indicates the median. The whiskers extend to the most extreme data points that are not considered outliers ($1.5 \times$ interquartile range). The vertical axis is omitted to aid visualization. See Supplementary Table 3 for details pertaining to each atlas.

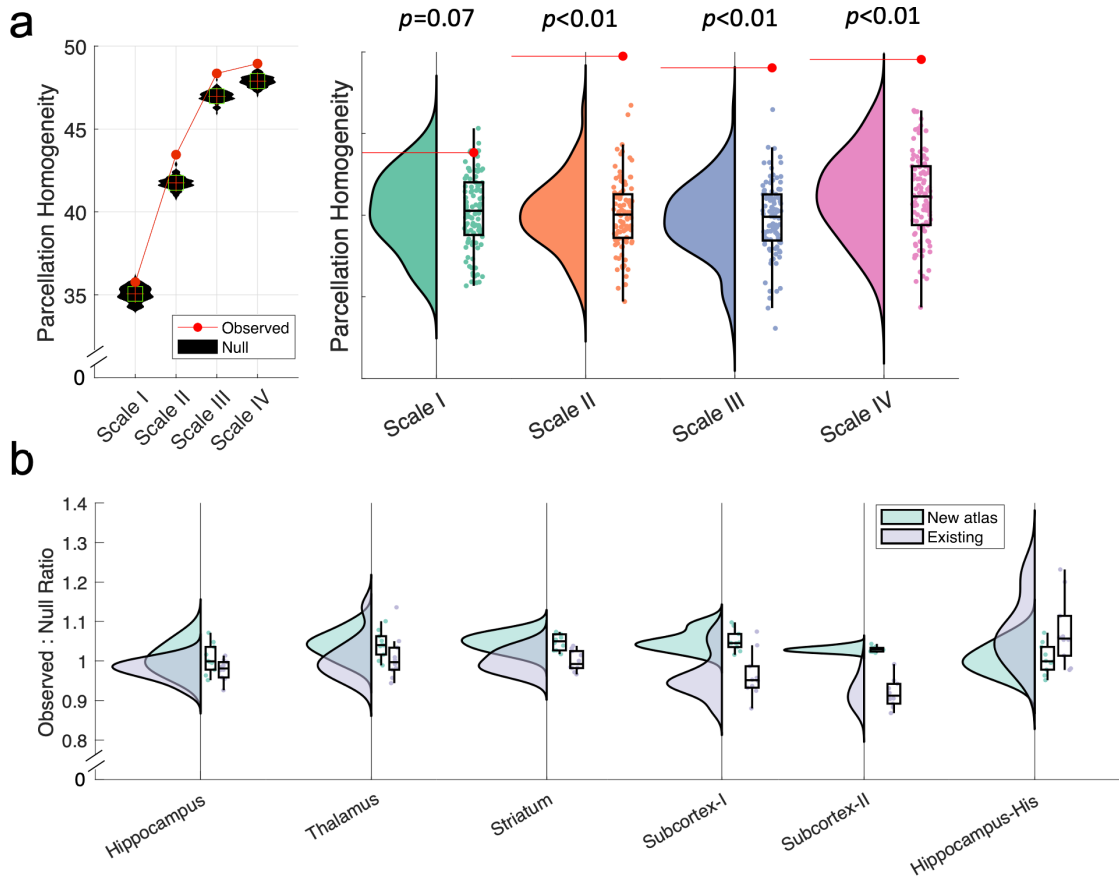


Figure 13. Parcellation homogeneity estimated in an independent validation dataset. Parcellation homogeneity was investigated in an independent dataset comprising 10 healthy individuals (Supplementary Table 1) to exclude potential circularity confounds. **a**, Parcellation homogeneity of the new subcortex atlas was estimated and benchmarked to random parcellations of the subcortex comprising an identical number of regions and a comparable distribution of region size. The same computations performed on the primary dataset were repeated on the validation dataset (see Methods and Figure 5). Violin plots show the distribution of parcellation homogeneity measured within ensemble of 100 random parcellations. One-sided p-value shown for each scale is the proportion of random parcellations comprising the ensemble that were more homogenous than the observe parcellation. Horizontal red lines indicate the observed parcellation homogeneity values. Bottom and top edges of the boxes indicate 25th and 75th percentiles of the distribution, respectively. The central mark indicates the median. Whiskers extend to the maximum and minimal data points that are not considered outliers. The vertical axis is omitted to aid visualization. The null hypothesis of parcellation homogeneity that is no better than chance could be rejected for all scales, except Scale I. **b**, Parcellation homogeneity comparison between the new atlas and existing parcellation atlases of the entire subcortex and specific subcortical nuclei (Supplementary Table 3). Parcellation homogeneity was computed separately for each individual ($n=10$) and normalized by the random parcellation homogeneity, yielding an observed-to-null ratio. The box plots show the distribution of this ratio across individuals for the new (turquoise) and existing (violet) parcellation atlases. Homogenous parcellations have a ratio that exceeds one. Bottom and top edges of the boxes indicate 25th and 75th percentiles of the distribution, respectively. The central mark indicates the median. The whiskers extend to the most extreme data points that are not considered outliers ($1.5 \times$ interquartile range).

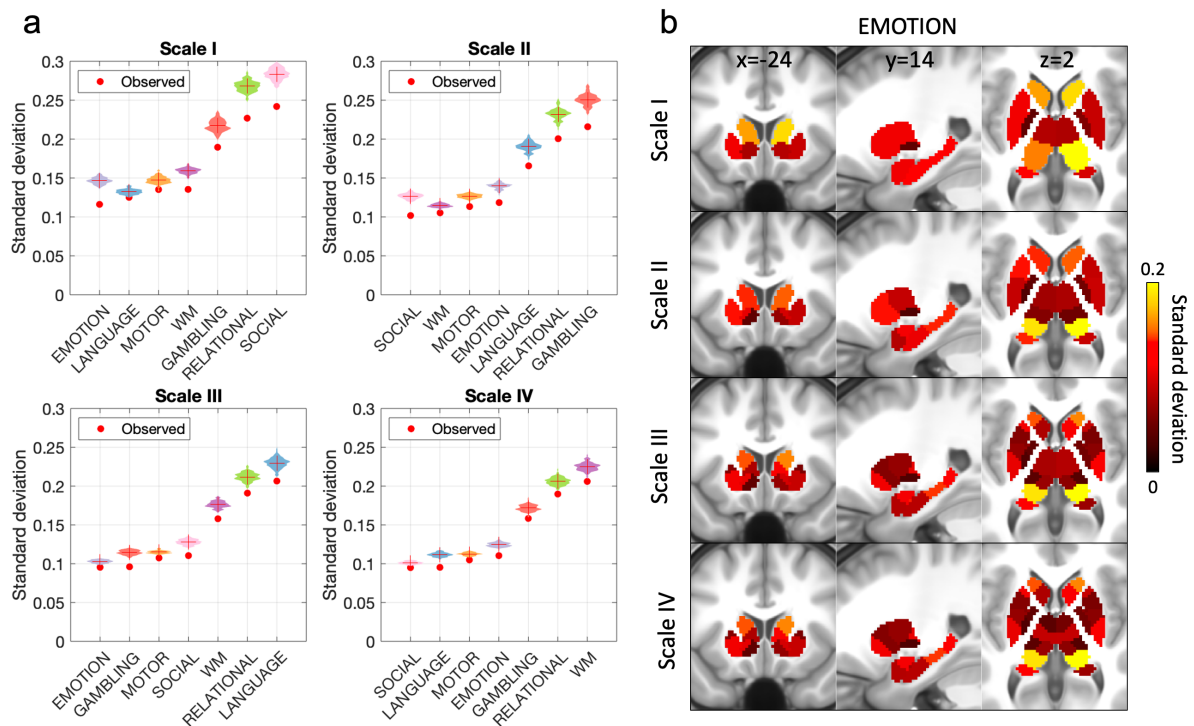


Figure 14. Quantifying the extent to which task-evoked activity is circumscribed to regions comprising the atlas for Scale I-IV. Task-evoked activity for seven distinct task conditions was computed by averaging over all blocked contrasts²¹ and across 997 individuals (<https://balsa.wustl.edu/>), yielding a group- and contrast-averaged effect size map (Cohen's d) for each task condition. **a**, The standard deviation in task-evoked activity (i.e. effect size maps) was computed across voxels comprising each region and then averaged over all regions. This was repeated for Scale I-IV. The lower the standard deviation, the more circumscribed task-evoked activity was to particular atlas regions. The standard deviation was computed in the same way for ensembles of random subcortical parcellations ($n=100$). This enabled testing of the null hypothesis that the extent to which task-evoked activity was circumscribed to specific atlas regions was no greater than expected for a random parcellation. Violin plots show the distribution of standard deviation computed within ensembles of 100 random parcellations and red dots indicate the observed standard deviation values. **b**, Examples of activation homogeneity in each region at Scale I-IV in the emotional processing task.

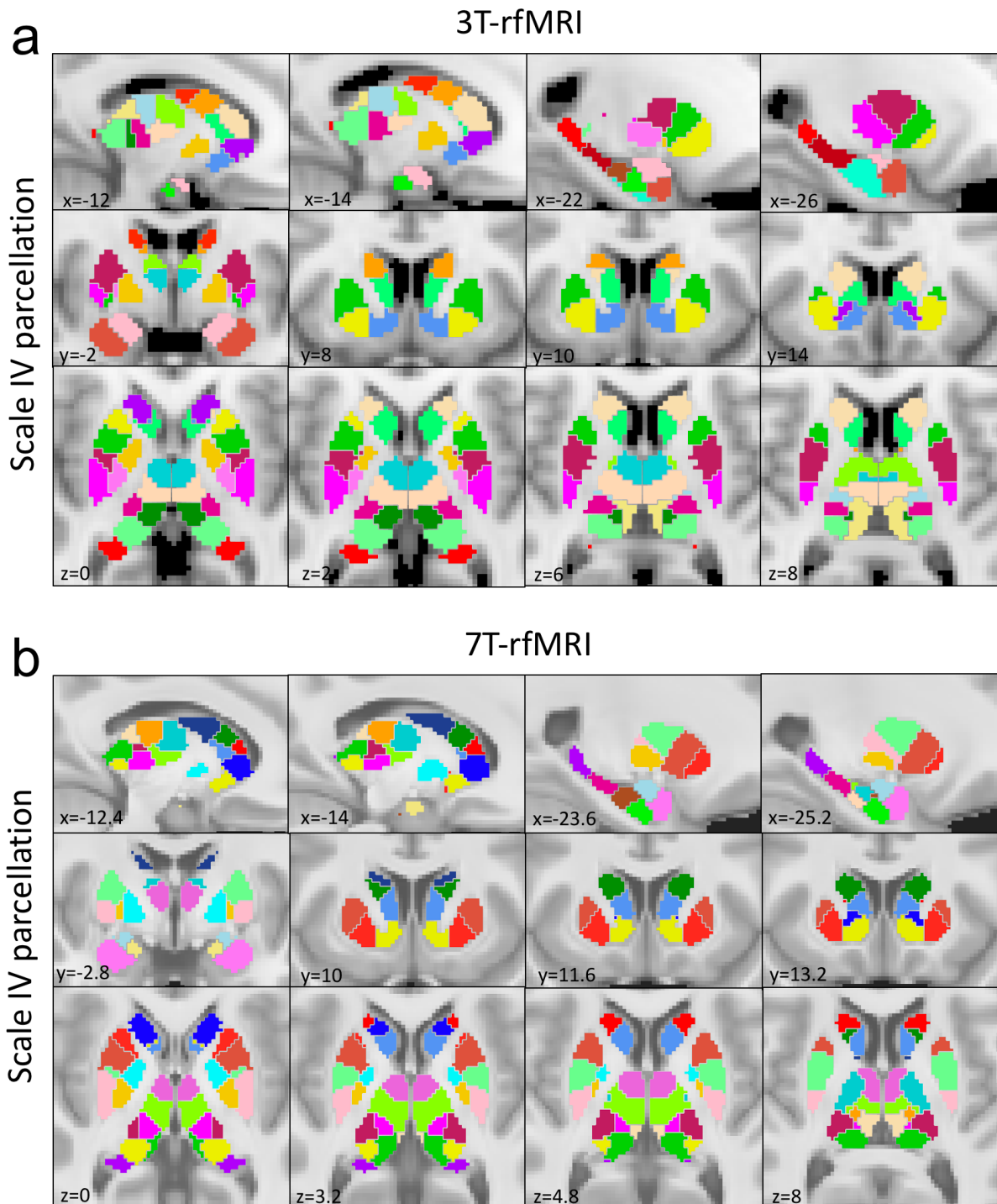


Figure 15. 3 Tesla and 7 Tesla subcortex parcellation at Scale IV. A total of four hierarchical scales were delineated using both 3T and 7T resting-state functional MRI (rfMRI) to parcellate the subcortex. Images show sagittal (x), coronal (y) and axial (z) slices from the group-consensus atlas at Scale IV delineated using 3T (**a**) and 7T (**b**) functional MRI. Scale IV at 3T comprises 27 bilateral regions, whereas Scale IV comprises 31 bilateral regions at 7T. The additional regions delineated at 7T include central and superior subregions of the medial amygdala, lateral and medial subregions of the hippocampal body, superior and inferior subregions of the lateral hippocampal head, and one more subregion in thalamus. All slice coordinates are indicated relative to MNI space (mm). A reference structural MRI image is used as the background. Homologous regions are colored identically.

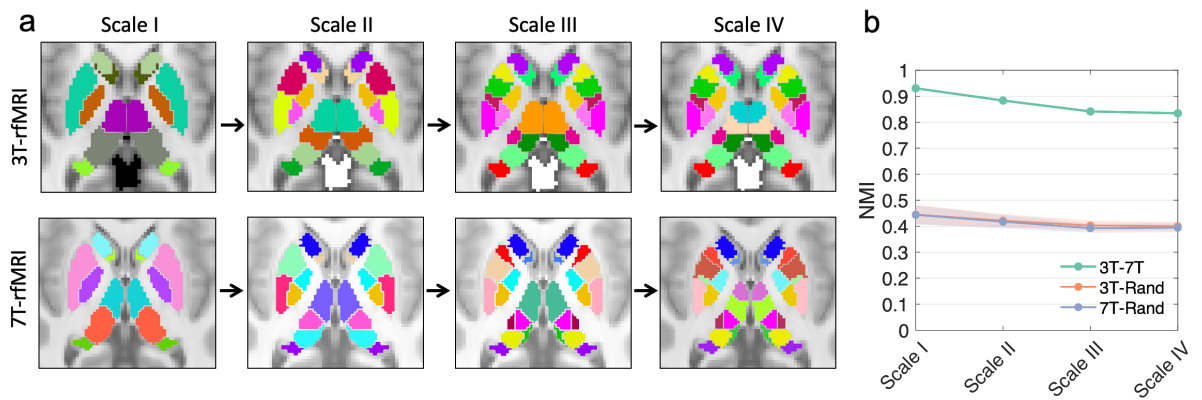


Figure 16. Quantitative comparison between 3 Tesla and 7 Tesla atlas across parcellation scales. **a**, Images show axial slices from the 3T and 7T group-consensus atlases across the four hierarchical parcellation scales (Scale I-IV, left to right). **b**, Spatial correspondence between the 3T and 7T atlas was estimated at each parcellation scale using normalized mutual information (NMI). NMI between 3T and 7T atlas (NMI, Scale I: 0.93; II: 0.88, III: 0.84, IV: 0.83, green) was benchmarked against ensembles of 100 random parcellations (3T-Rand, orange; 7T-Rand, blue) at each parcellation scale. Shading indicates 95% confidence intervals. NMI ranges from zero to one with higher value indicating greater spatial correspondence. The 3T atlas (2mm isotropic) was up-sampled to the same resolution as 7T (1.6mm isotropic) before computing NMI.

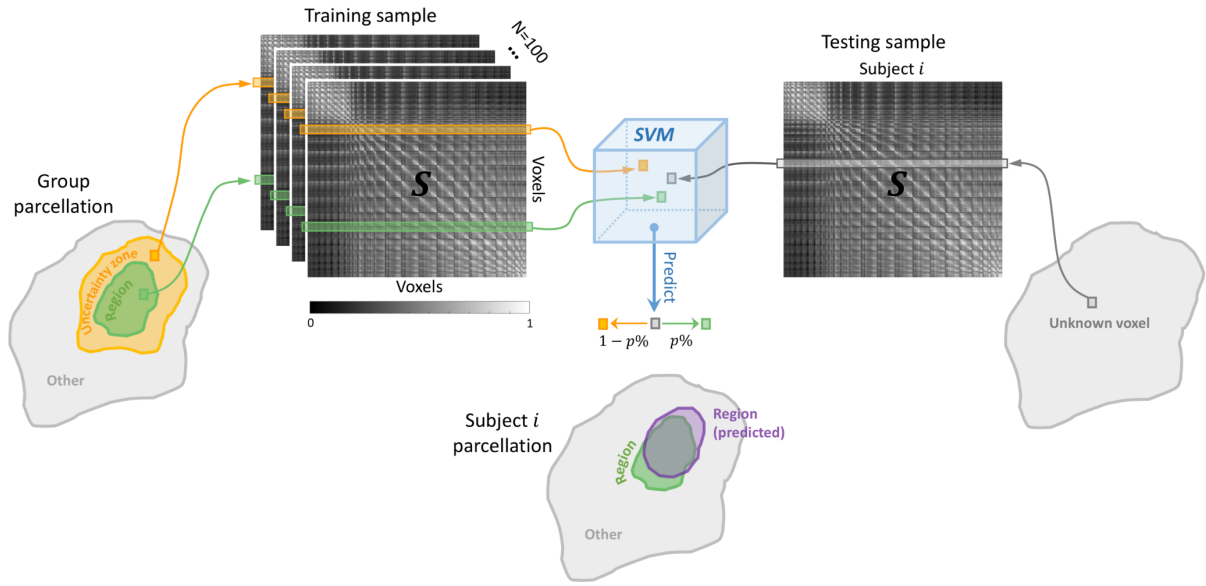


Figure 17. Schematic of methodology for parcellation personalization. A binary support vector machine (SVM) classifier (blue box) was trained to classify whether a voxel resided in the region proper (green) or its uncertainty zone (orange). The SVM feature space was defined over the similarity matrix (S), where each cell stored the similarity in functional connectivity between a pair of subcortical voxels. The feature for a particular voxel was selected as the relevant row in this matrix, highlighted by green and orange colored strips. One hundred randomly selected individuals were used to train a separate SVM classifier for each region. The uncertainty zone for each region was delineated by dilating the region's mask (see Methods). For a new individual (Subject i), the trained classifier was used to predict the posterior probability ($p\%$) of an unknown voxel (gray) belonging to the region as opposed to belonging to the region's uncertainty zone ($1 - p\%$). This was repeated for each region comprising the Scale IV atlas. The uncertainty zones of two distinct regions could potentially overlap, meaning that voxels could be assigned a probability of belonging to multiple regions. Such voxels were assigned to the region associated with the highest posterior probability, yielding a personalized parcellation atlas for Subject i (purple).

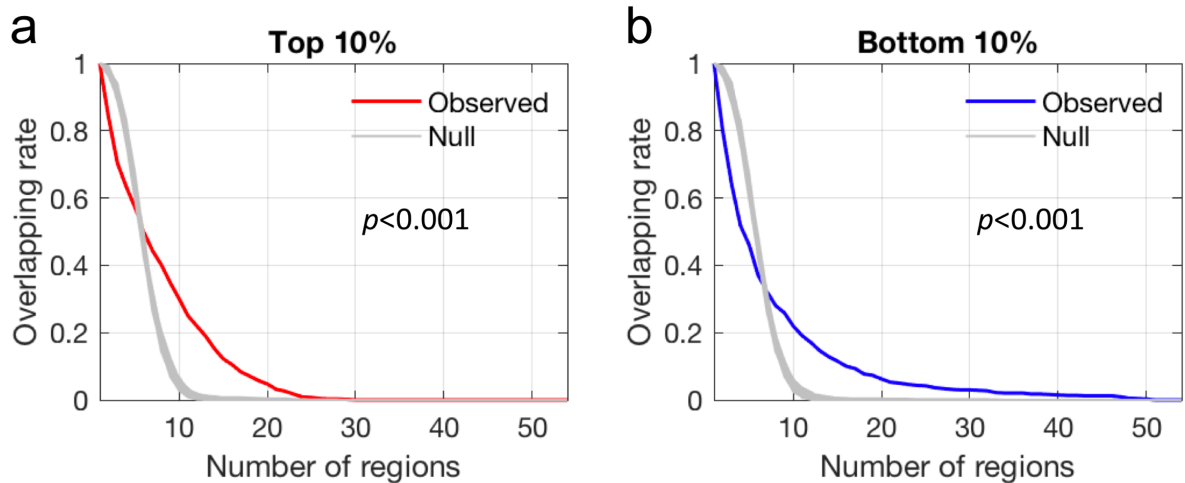


Figure 18. Within-subject variation in Dice coefficient across subcortical regions. The Dice coefficient for each Scale IV subcortical region in each individual was encoded in a Dice-matrix of dimension 921×54 , where 921 is the total number individuals and 54 is the number of subcortical regions. Rows in this matrix were then re-ordered from the highest to lowest Dice coefficient. This re-ordering was performed separately for each column. Individuals ranked among the top 10% (high Dice) or bottom 10% (low Dice) for at least one column (region) were selected, yielding 696 and 739 unique individuals in each group, respectively. Some individuals only presented once, whereas some individuals repeatedly presented in more than one region. The proportions of individuals (overlapping rate) that repeatedly presented in at least one or more subcortical regions were computed. The curves show the overlapping rate as a functional of the number of regions in the high Dice (**a**, red curve) and low Dice (**b**, blue curve) group separately. The area under the curve of the overlapping rate was computed. Permutation testing ($n=1000$) was used to test whether the overlapping rate was larger than expected due to chance. Note that each row in the Dice-matrix was shuffled as a whole in each permutation to control the relationship across regions. The overlapping rate was recomputed for each permuted sample and plotted as a functional of number of regions (Null, gray curves). The one-sided p-values shown are given by the proportion of null curves that had larger area under the curve than the observed curve.

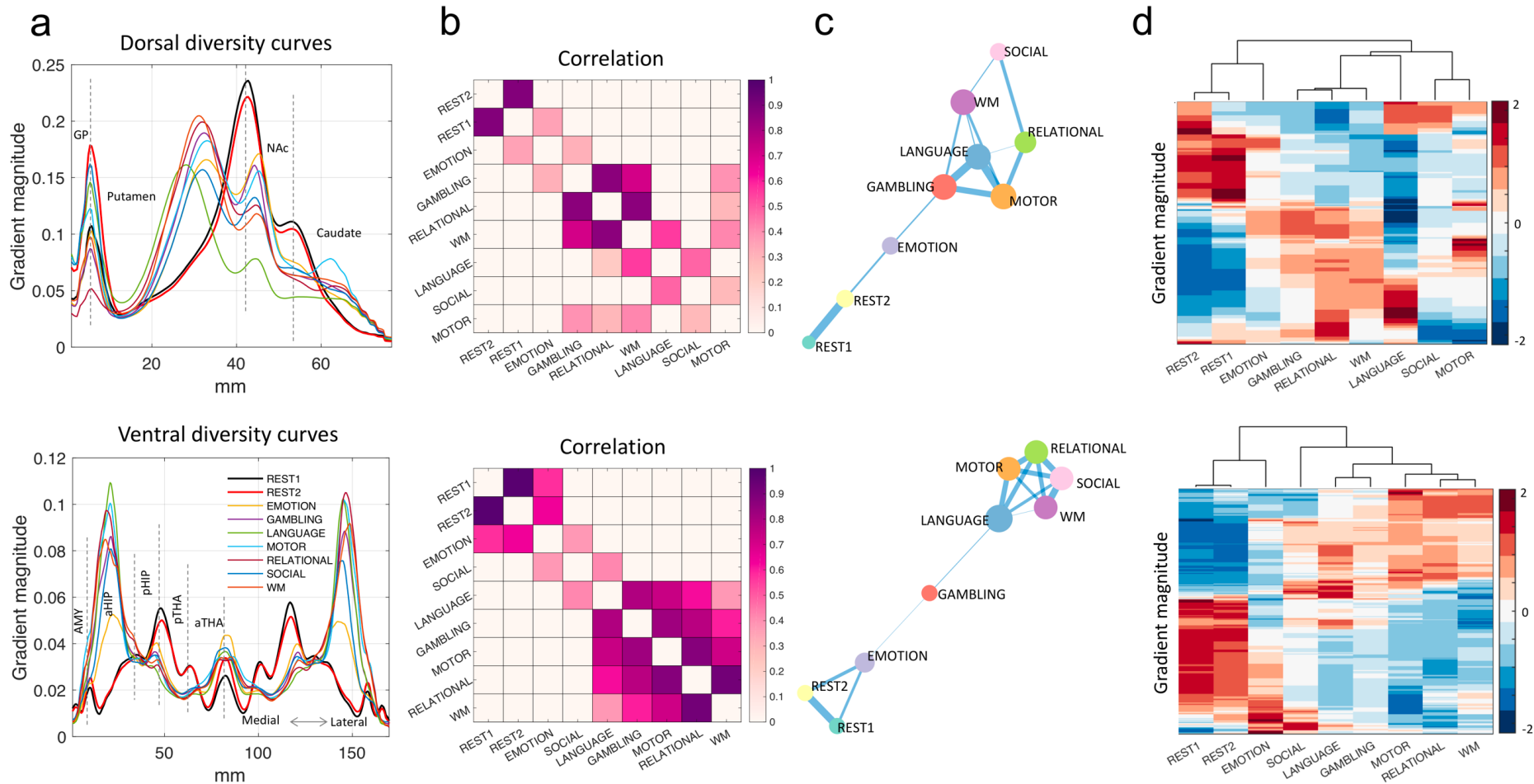


Figure 19. Variation in subcortical connectivity gradients between rest and task-evoked conditions. a, Dorsal and ventral diversity curves are shown for each rest and task condition separately. **b,** Similarity in the diversity curves between each pair of conditions was estimated using the Pearson correlation coefficient. Permutation testing ($n=10,000$) was used to determine the significance (p -value) of each correlation coefficient using a corrected significance threshold of $p < 0.05/36=0.0014$ (Bonferroni correction). Correlation coefficients surviving Bonferroni correction are colored in the matrix shown and also visualized as a graph. **c,** In the graph, each node represents one

of the nine conditions and the edges between them indicate correlations. Node size is scaled by nodal degree, whereas edge thickness varies according to the correlation coefficient magnitude. **d**, Matrix representation of diversity curves for rest and task conditions. Matrix rows correspond to specific points along the diversity curves. Matrix columns correspond to rest and task conditions. Rows and columns are reordered to accentuate similarity between diversity curves. Average-linkage clustering was used to determine the reordering and the cluster tree shown.

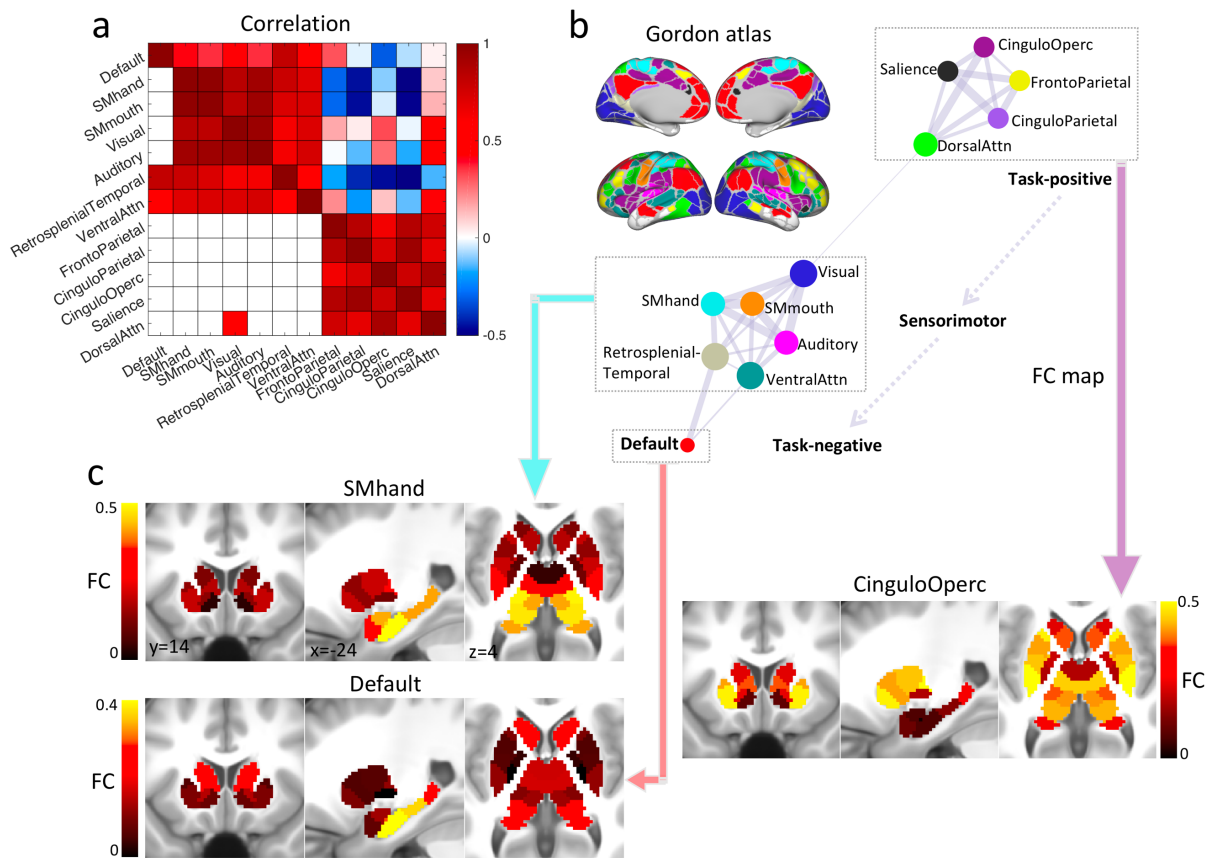


Figure 20. Linking canonical cortical networks based on their functional connectivity with subcortical regions.

Functional connectivity (FC) was computed between each Scale IV subcortical region and each cortical parcel delineated in an existing cortical atlas²⁰, yielding a connectivity matrix of dimension 54 x 333 for each individual. The connectivity matrices were then averaged across all individuals (REST1, n=1080) to enable a group-consensus representation of cortical-subcortical connectivity. Each column in this matrix thus represents a subcortical connectivity map for a given cortical parcel. Subcortical connectivity maps were averaged across cortical parcels that belong to the same canonical network²⁰, yielding 12 FC maps that represent how each cortical network connects to the subcortex. The 12 networks are as follows: visual, dorsal somatomotor (SMmouth), ventral somatomotor (SMhand), auditory, default, frontoparietal, dorsal attention, ventral attention, cingulo-opercular (cinguloOperc), salience, cingulo-parietal and retrosplenial-temporal network. **a**, Similarity in subcortical FC maps between each pair of cortical networks was estimated using the Pearson correlation coefficient, yielding a 12×12 correlation matrix. The rows and columns of this matrix were reordered to accentuate modular structure, which was determined by the Louvain community detection algorithm²². The 12 × 12 correlation matrix was thresholded using a statistical approach based on null hypothesis testing. A p-value was computed for each correlation coefficient as follows. Permutation testing (n=1000) was used to determine the significance (p-value) of each correlation coefficient using a corrected significance threshold of $p<0.05/66=0.008$ (Bonferroni correction). Correlation coefficients that survived correction are shown in the lower triangle of the correlation matrix and visualized as a graph. **b**, In this graph, each node represents a canonical cortical network. Edges are drawn between pairs of networks that share common patterns of functional connectivity with subcortical regions. Node size is scaled by nodal degree, whereas edge thickness

varies according to the correlation coefficient. Nodes were parsed into three groups (gray blocks) and positioned on a task-positive to task-negative organizational axis. **C**, Representative subcortical FC maps for each group of canonical networks. It can be seen that the cingulo-opercular network (task-positive) is preferentially connected to thalamus and striatum, especially the dorsal striatum. In contrast, sensorimotor networks are predominantly connected to the hippocampus, amygdala and posterior thalamus. The default mode network (task-negative) is preferentially connected to the hippocampus but also show moderate connectivity with posterior thalamus and caudate.

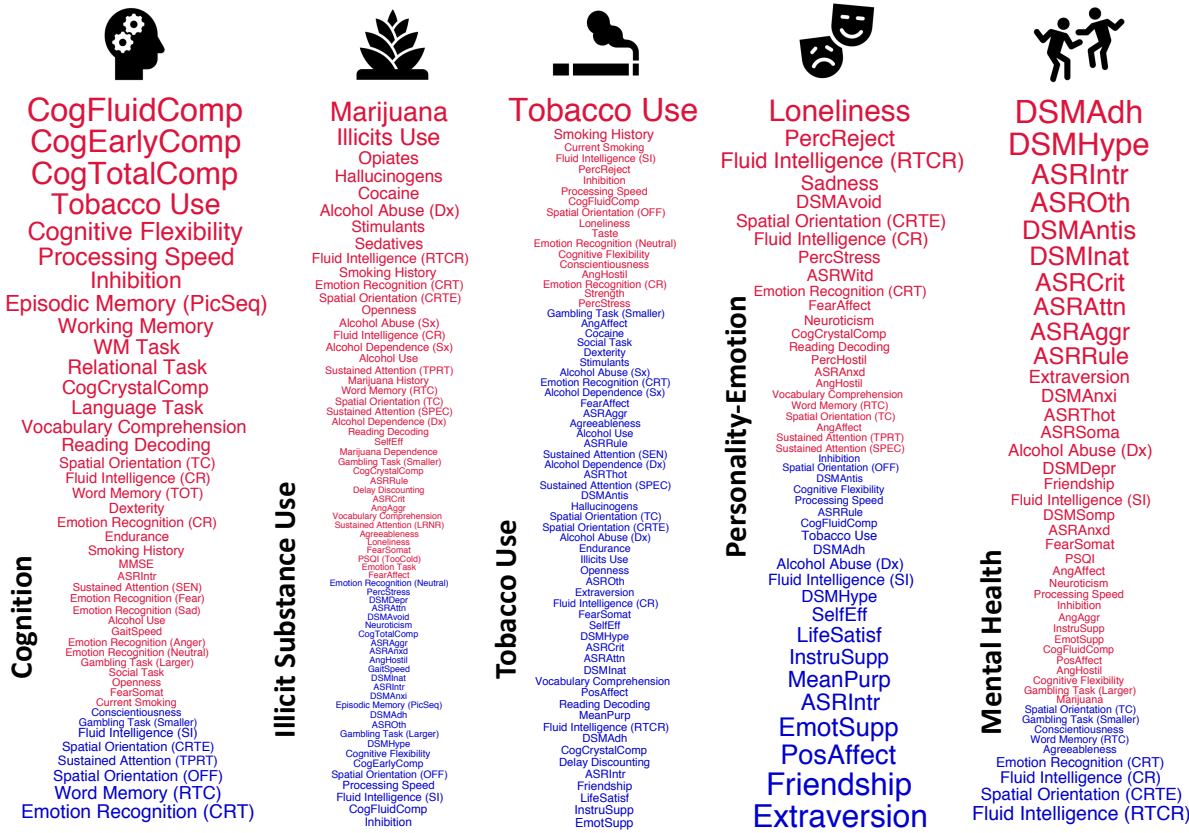


Figure 21. Behavioral dimensions. Five orthogonal behavioral dimensions characterizing: i) cognition, ii) illicit substance use, iii) tobacco use, iv) personality and emotion traits, as well as v) mental health were derived from a total of 109 behavioral items using independent component analysis (see Methods). The top weighted (30-40%) behavioral items in each dimension are visualized as word clouds. The font size of each item is scaled according to its absolute weight in the ICA de-mixing matrix, and the font color denotes weight polarity (red-positive, blue-negative).

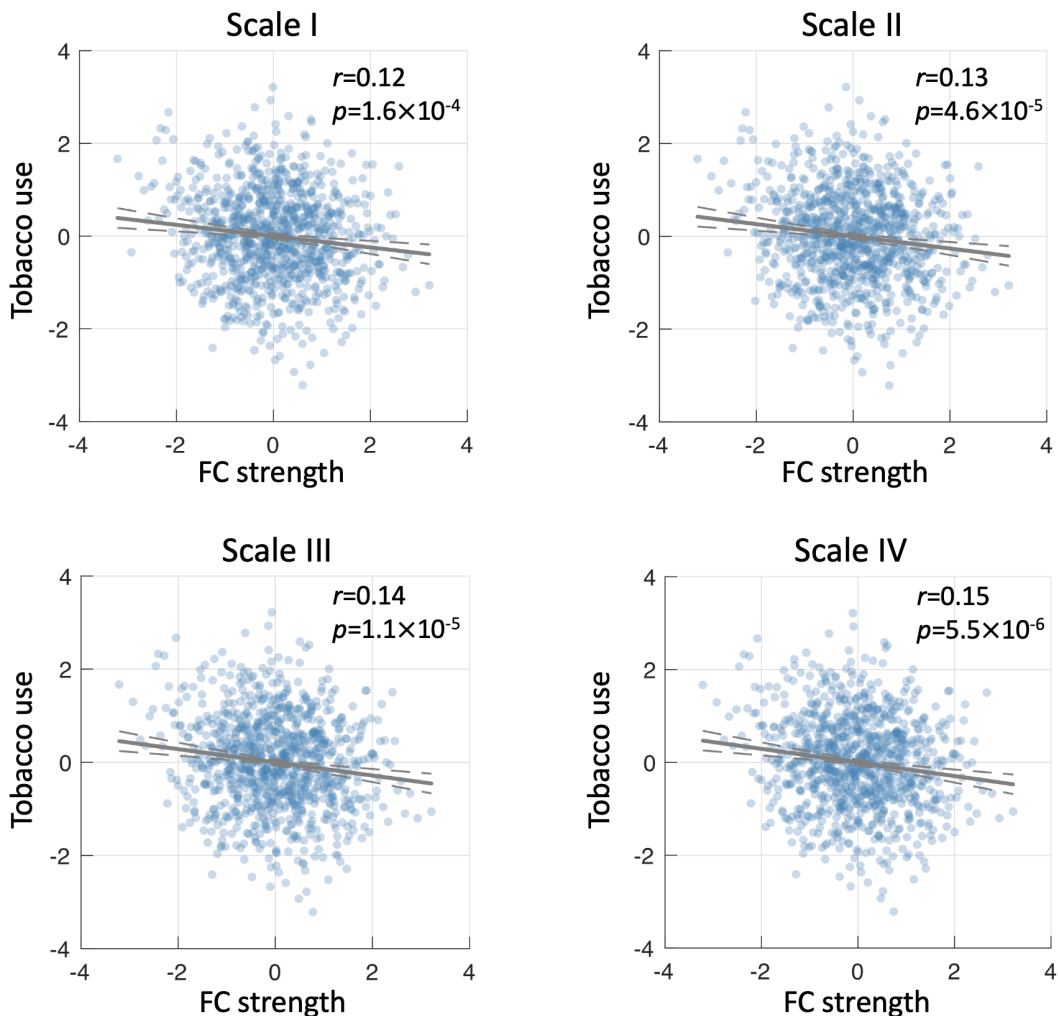


Figure 22. Association between subcortical functional connectivity and the behavioral dimension characterizing tobacco use reproduced using functional MRI from a second session. Scatter plots and lines of best fit show the association between individual variation in tobacco use dimension and functional connectivity (FC) strength within the thalamo-striato-hippocampal network measured using functional MRI acquired in the REST1 session. The significant association was discovered using functional MRI acquired in REST2 (see Figure 8). Each blue dot in the scatter plot represents one individual ($n=958$). Solid gray lines indicate lines of best fit. Dashed lines indicate 95% confidence intervals. R-values are the Pearson correlation coefficients and p-values assess the null hypothesis of zero correlation. The association between subcortical functional connectivity and tobacco use was reproducible across independent functional MRI sessions (REST1 and REST2) and across parcellation scales (Scale I-IV).

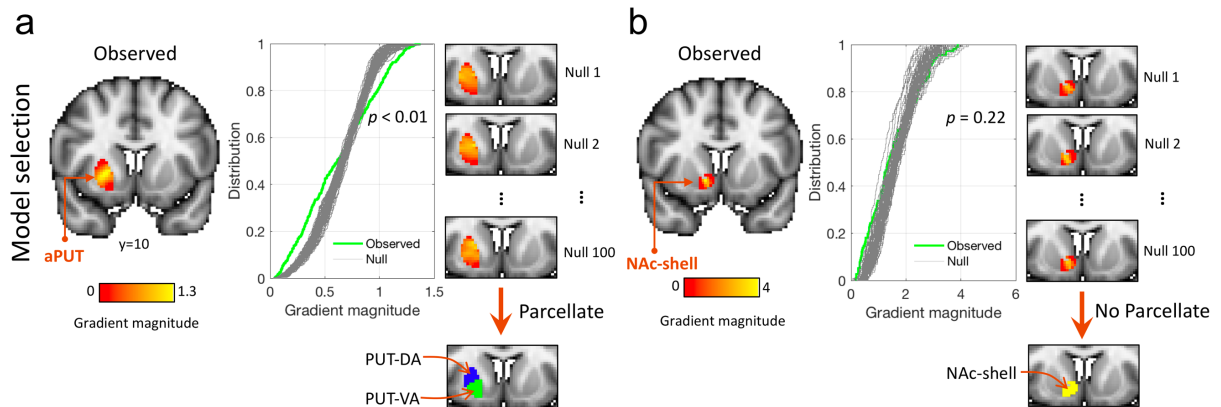


Figure 23. Model selection with Kolmogorov-Smirnov (KS) test. **a**, Gradient magnitude image for anterior putamen (aPUT) is shown as a coronal slice (left). The yellow colored strip within the aPUT indicates a gradient magnitude peak, suggesting the location of a putative boundary. The KS test suggests that the gradient magnitude distribution across the voxels in this region (green curve) is significantly longer tailed than the null data (gray curves, $n=100$, $p<0.01$, one-sided). Therefore, a boundary was delineated that resulted in parcellation of the anterior putamen into one dorsal (PUT-DA, blue) and one ventral (PUT-VA, green) component. **b**, KS test for the shell of the nucleus accumbens (NAc-shell). Although a strong gradient is evident, the null hypothesis could not be rejected with the KS test ($p=0.22$, one-sided), and thus subdivision of NAc-shell was not warranted.

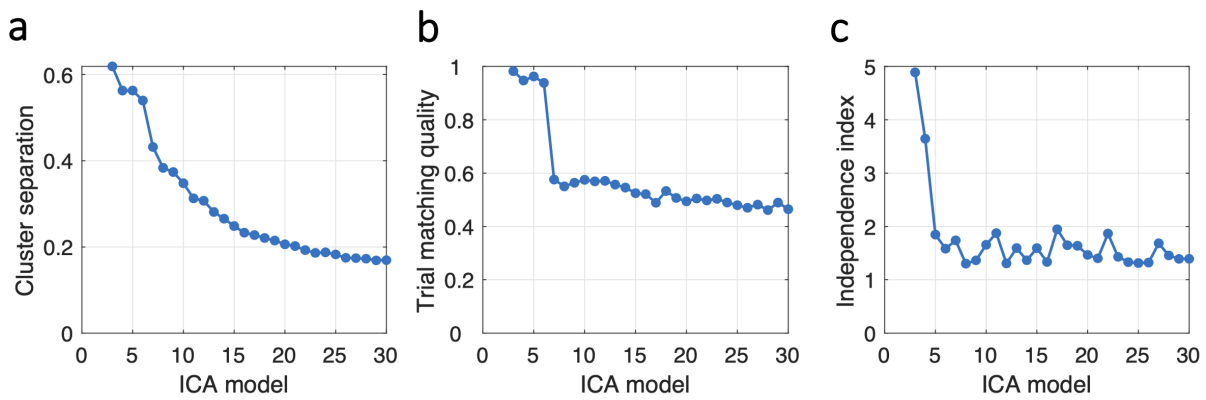


Figure 24. Determining the optimal number of independent components. Independent component analysis (ICA) was used to decompose a total of 109 behavioral measures into a set of latent behavioral dimensions. ICA performance for candidate ICA models (i.e. total number of components) ranging from 3 to 30 was evaluated based on cluster separation (**a**), trial matching quality (**b**) and independence index (**c**). Each measure was computed as a function of the total number of components and selection of the optimal model was guided by identifying abrupt changes in these measures as a function of the ICA model.

Supplementary Tables

Table 1. Basic demographic characteristics and acquisition details

Dataset	Modality	Magnetic field	Sample size	Age (mean \pm std yrs)	Sex (M/F)
3T-rfMRI (REST1)	Resting-state	3 Tesla	1080	28.8 \pm 3.7	495/585
3T-rfMRI (REST2)	Resting-state	3 Tesla	1021	28.7 \pm 3.7	471/550
7T-rfMRI	Resting-state	7 Tesla	183	29.4 \pm 3.3	72/111
tfMRI	Task-evoked	3 Tesla	725	28.7 \pm 3.7	360/365
Independent validation dataset	Resting-state	3 Tesla	10	26.0 \pm 2.1	6/4

Table 2. Nomenclature for 3T parcellation hierarchy

Name	Abbreviation	Name	Abbreviation
Hippocampus	HIP	Amygdala	AMY
Anterior hippocampus	aHIP	Lateral amygdala	lAMY
Hippocampus head, medial division	HIP-head-m	Medial amygdala	mAMY
Subdivision1	HIP-head-m1	Caudate nucleus	CAU
Subdivision2	HIP-head-m2	Anterior caudate	aCAU
Hippocampus head, lateral division	HIP-head-l	Dorsoanterior caudate	CAU-DA
Posterior hippocampus	pHIP	Ventroanterior caudate	CAU-VA
Hippocampus body	HIP-body	Posterior caudate	pCAU
Hippocampus tail	HIP-tail	Caudate tail	CAU-tail
Thalamus	THA	Caudate body	CAU-body
Anterior thalamus	aTHA	Nucleus accumbens*	NAc
Dorsoanterior thalamus	THA-DA	Nucleus accumbens, shell	NAc-shell
Lateral dorsoanterior thalamus	THA-DAI	Nucleus accumbens, core	NAc-core
Medial dorsoanterior thalamus	THA-DAm	Putamen	PUT
Ventroanterior thalamus	THA-VA	Anterior putamen	aPUT
Superior ventroanterior thalamus	THA-Vas	Dorsoanterior putamen	PUT-DA
Inferior ventroanterior thalamus	THA-VAi	Ventroanterior putamen	PUT-VA
Anterior division	THA-VAia	Posterior putamen	pPUT
Posterior division	THA-VAip	Dorsoposterior putamen	PUT-DP
Posterior thalamus	pTHA	Ventroposterior putamen	PUT-VP
Dorsoposterior thalamus	THA-DP	Globus pallidus	GP
Ventroposterior thalamus	THA-VP	Anterior globus pallidus	aGP
Medial ventroposterior thalamus	THA-VPm	Posterior globus pallidus	pGP
Lateral ventroposterior thalamus	THA-VPl		

*The nucleus accumbens subdivisions bear moderate resemblance to the anatomical shell and core of the NAc and have thus been named as such. However, this correspondence was not formally tested.

Table 3. Comparison parcellation atlases of the human subcortex and specific subcortical nuclei

Atlas	Study	Modality	Metric	Number of regions
Hippocampus	Plachti et al. 2019 ²³	Resting-state fMRI	Functional connectivity	5
Thalamus	Behrens et al. 2003 ²⁴	Diffusion MRI	Tractography	7
Striatum	Janssen et al. 2015 ²⁵	Resting-state fMRI	Functional connectivity	6
Subcortex-I	Ji et al. 2019 ²⁶	Resting-state fMRI	Functional connectivity	12
Subcortex-II	Fan et al. 2016 ²⁷	Diffusion MRI	Tractography	36
Hippocampus - His	Amunts et al 2005 ¹¹ ; Eickhoff et al 2005 ¹²	Histology	Cytoarchitecture	3

Table 4. List of 109 selected behavioral items

Category	Formal Name	Intuitive Name	Psychological Test
Alertness	MMSE_Score	MMSE	Mini Mental Status Exam
	PSQI_Score	PSQI	Pittsburgh Sleep Questionnaire
	PSQI_TooCold	PSQI (TooCold)	Pittsburgh Sleep Questionnaire
	PSQI_TooHot	PSQI (TooHot)	Pittsburgh Sleep Questionnaire
	PSQI_BadDream	PSQI (BadDream)	Pittsburgh Sleep Questionnaire
	PSQI_Pain	PSQI (Pain)	Pittsburgh Sleep Questionnaire
Cognition	PicSeq_Unadj	Episodic Memory (PicSeq)	NIH Toolbox Picture Sequence Memory Test
	CardSort_Unadj	Cognitive Flexibility	NIH Toolbox Dimensional Change Card Sort
	Flanker_Unadj	Inhibition	NIH Toolbox Flanker Inhibitory Control and Attention
	PMAT24_A_CR	Fluid Intelligence (CR)	Penn Progressive Matrices
	PMAT24_A_SI	Fluid Intelligence (SI)	Penn Progressive Matrices
	PMAT24_A_RTCR	Fluid Intelligence (RTCR)	Penn Progressive Matrices
	ReadEng_Unadj	Reading Decoding	NIH Toolbox Oral Recognition Test
	PicVocab_Unadj	Vocabulary Comprehension	NIH Toolbox Picture Vocabulary Test
	ProcSpeed_Unadj	Processing Speed	NIH Toolbox Pattern Comparison Processing Speed Test
	DDisc_AUC_200	Delay Discounting	Delay Discounting
	VSPLIT_TC	Spatial Orientation (TC)	Variable Short Penn Line Orientation
	VSPLIT_CRT	Spatial Orientation (CRT)	Variable Short Penn Line Orientation
	VSPLIT_OFF	Spatial Orientation (OFF)	Variable Short Penn Line Orientation
	SCPT_TPRT	Sustained Attention (TPRT)	Short Penn Continuous Performance Test
	SCPT_SEN	Sustained Attention (SEN)	Short Penn Continuous Performance Test
	SCPT_SPEC	Sustained Attention (SPEC)	Short Penn Continuous Performance Test
	SCPT_LRNR	Sustained Attention (LRNR)	Short Penn Continuous Performance Test
	IWRD_TOT	Word Memory (TOT)	Penn Word Memory Test
	IWRD_RTC	Word Memory (RTC)	Penn Word Memory Test
Emotion	ListSort_Unadj	Working Memory	NIH Toolbox List Sorting Working Memory Test
	CogFluidComp_Unadj	CogFluidComp	NIH Toolbox Cognition Fluid Composite
	CogEarlyComp_Unadj	CogEarlyComp	NIH Toolbox Cognition Early Childhood Composite
	CogTotalComp_Unadj	CogTotalComp	NIH Toolbox Cognition Total Composite Score
	CogCrystalComp_Unadj	CogCrystalComp	NIH Toolbox Cognition Crystallized Composite
	ER40_CR	Emotion Recognition (CR)	Penn Emotion Recognition Test
	ER40_CRT	Emotion Recognition (CRT)	Penn Emotion Recognition Test
	ER40ANG	Emotion Recognition (Anger)	Penn Emotion Recognition Test
	ER40FEAR	Emotion Recognition (Fear)	Penn Emotion Recognition Test
Hostile/Affective	ER40HAP	Emotion Recognition (Happy)	Penn Emotion Recognition Test
	ER40NOE	Emotion Recognition (Neutral)	Penn Emotion Recognition Test
	ER40SAD	Emotion Recognition (Sad)	Penn Emotion Recognition Test
	AngAffect_Unadj	AngAffect	NIH Toolbox Anger-Affect Survey
	AngHostil_Unadj	AngHostil	NIH Toolbox Anger-Hostility Survey

	AngAggr_Unadj	AngAggr	NIH Toolbox Anger-Physical Aggression Survey
	FearAffect_Unadj	FearAffect	NIH Toolbox Fear-Affect Survey
	FearSomat_Unadj	FearSomat	NIH Toolbox Fear-Somatic Arousal Survey
	Sadness_Unadj	Sadness	NIH Toolbox Sadness Survey
Emotion	LifeSatisf_Unadj	LifeSatisf	NIH Toolbox General Life Satisfaction Survey
	MeanPurp_Unadj	MeanPurp	NIH Toolbox Meaning and Purpose Survey
	PosAffect_Unadj	PosAffect	NIH Toolbox Positive Affect Survey
	Friendship_Unadj	Friendship	NIH Toolbox Friendship Survey
	Loneliness_Unadj	Loneliness	NIH Toolbox Loneliness Survey
	PercHostil_Unadj	PercHostil	NIH Toolbox Perceived Hostility Survey
	PercReject_Unadj	PercReject	NIH Toolbox Perceived Rejection Survey
	EmotSupp_Unadj	EmotSupp	NIH Toolbox Emotional Support Survey
	InstruSupp_Unadj	InstruSupp	NIH Toolbox Instrumental Support Survey
	PercStress_Unadj	PercStress	NIH Toolbox Perceived Stress Survey
	SelfEff_Unadj	SelfEff	NIH Toolbox Self-Efficacy Survey
	Endurance_Unadj	Endurance	NIH Toolbox 2-minute Walk Endurance Test
Motor	GaitSpeed_Comp	GaitSpeed	NIH Toolbox 4-Meter Walk Gait Speed Test
	Dexterity_Unadj	Dexterity	NIH Toolbox 9-hole Pegboard Dexterity Test
	Strength_Unadj	Strength	NIH Toolbox Grip Strength Test
	NEOFAC_A	Agreeableness	NEO-FFI
Personality	NEOFAC_O	Openness	NEO-FFI
	NEOFAC_C	Conscientiousness	NEO-FFI
	NEOFAC_N	Neuroticism	NEO-FFI
	NEOFAC_E	Extraversion	NEO-FFI
	Odor_Unadj	Odor	NIH Toolbox Odor Identification Scale
Sensory	PainInterf_Tscore	PainInterf	NIH Toolbox Pain Interference Survey
	Taste_Unadj	Taste	NIH Toolbox Regional Taste Intensity
	Mars_Final	Visual Contrast Sensitivity	Mars Contrast Sensitivity Score
	DSM_Depr_Raw	DSMDepr	ASR-DSM
	DSM_Anxi_Raw	DSMANxi	ASR-DSM
	DSM_Somp_Raw	DSMSomp	ASR-DSM
	DSM_Avoid_Raw	DSMAvoid	ASR-DSM
	DSM_Adh_Raw	DSMAdh	ASR-DSM
	DSM_Inat_Raw	DSMInat	ASR-DSM
	DSM_Hype_Raw	DSMHype	ASR-DSM
	DSM_Antis_Raw	DSMAntis	ASR-DSM
Psychiatric and Life Function	ASR_Anxd_Raw	ASRAnxd	ASR-DSM
	ASR_Witd_Raw	ASRWitd	ASR-DSM
	ASR_Soma_Raw	ASRSoma	ASR-DSM
	ASR_Thot_Raw	ASRThot	ASR-DSM
	ASR_Attn_Raw	ASRAttn	ASR-DSM
	ASR_Aggr_Raw	ASRAggr	ASR-DSM

	ASR_Rule_Raw	ASRRule	ASR-DSM
	ASR_Intr_Raw	ASRIintr	ASR-DSM
	ASR_Oth_Raw	ASROth	ASR-DSM
	ASR_Crit_Raw	ASRCrit	ASR-DSM
	Num_Days_Drank_7days	Alcohol Use	Alcohol Use 7-Day Retrospective
	SSAGA_Alcohol_D4_Dp_Sx	Alcohol Dependence (Sx)	Alcohol Use and Dependence
	SSAGA_Alcohol_D4_Ab_Dx	Alcohol Abuse (Dx)	Alcohol Use and Dependence
	SSAGA_Alcohol_D4_Ab_Sx	Alcohol Abuse (Sx)	Alcohol Use and Dependence
	SSAGA_Alcohol_D4_Dp_Dx	Alcohol Dependence (Dx)	Alcohol Use and Dependence
	Num_Days_Used_Any_Tobacco_7days	Tobacco Use	Tobacco Use 7-Day Retrospective
	SSAGA_TB_Smoking_History	Smoking History	Tobacco Use and Dependence
	SSAGA_TB_Still_Smoking	Current Smoking	Tobacco Use and Dependence
	SSAGA_Times_Used_Illlicit	Illicit Use	Illicit Drug Use
Substance Use	SSAGA_Times_Used_Cocaine	Cocaine	Illicit Drug Use
Use	SSAGA_Times_Used_Hallucinogens	Hallucinogens	Illicit Drug Use
	SSAGA_Times_Used_Opiates	Opiates	Illicit Drug Use
	SSAGA_Times_Used_Sedatives	Sedatives	Illicit Drug Use
	SSAGA_Times_Used_Stimulants	Stimulants	Illicit Drug Use
	SSAGA_Marijuana_Use	Marijuana History	Marijuana Use and Dependence
	SSAGA_Marijuana_Abuse_Dep	Marijuana Dependence	Marijuana Use and Dependence
	SSAGA_Marijuana_Times_Used	Marijuana	Marijuana Use and Dependence
	Emotion_Task_Acc	Emotion Task	In-Scanner Task Performance
	Gambling_Task_Perc_Larger	Gambling Task (Larger)	In-Scanner Task Performance
	Gambling_Task_Perc_Smaller	Gambling Task (Smaller)	In-Scanner Task Performance
In-Scanner Task	Language_Task_Acc	Language Task	In-Scanner Task Performance
Task	Relational_Task_Acc	Relational Task	In-Scanner Task Performance
	Social_Task_Perc_TOM	Social Task	In-Scanner Task Performance
	WM_Task_Acc	WM Task	In-Scanner Task Performance

Table 5. NIFTI and CIFTI file names for 3T and 7T atlas

Magnetic strength	Scale	Number of regions	Spatial resolution (mm) ^a	File name ^b
3 Tesla	I	16	2×2×2	Tian_Subcortex_S1_3T.nii Tian_Subcortex_S1_3T_dscalar.nii
	II	32		Tian_Subcortex_S2_3T.nii Tian_Subcortex_S2_3T_dscalar.nii
	III	50		Tian_Subcortex_S3_3T.nii Tian_Subcortex_S3_3T_dscalar.nii
	IV	54		Tian_Subcortex_S4_3T.nii Tian_Subcortex_S4_3T_dscalar.nii
7 Tesla	I	16	1.6×1.6×1.6	Tian_Subcortex_S1_7T.nii Tian_Subcortex_S1_7T_dscalar.nii
	II	34		Tian_Subcortex_S2_7T.nii Tian_Subcortex_S2_7T_dscalar.nii
	III	54		Tian_Subcortex_S3_7T.nii Tian_Subcortex_S3_7T_dscalar.nii
	IV	62		Tian_Subcortex_S4_7T.nii Tian_Subcortex_S4_7T_dscalar.nii

a, Atlas is in MNI standard space (MNI ICBM 152 nonlinear 6th generation)

b, NIFTI: *.nii; CIFTI: *dscalar.nii. Atlas is openly available at: <https://github.com/yetianmed/subcortex>

Supplementary References

1. Collins, C.E., Airey, D.C., Young, N.A., Leitch, D.B. & Kaas, J.H. Neuron densities vary across and within cortical areas in primates. *Proceedings of the National Academy of Sciences* **107**, 15927-15932 (2010).
2. Cahalane, D.J., Charvet, C.J. & Finlay, B.L. Systematic, balancing gradients in neuron density and number across the primate isocortex. *Front Neuroanat* **6**, 28 (2012).
3. Charvet, C.J., Cahalane, D.J. & Finlay, B.L. Systematic, Cross-Cortex Variation in Neuron Numbers in Rodents and Primates. *Cerebral Cortex* **25**, 147-160 (2013).
4. Charvet, C.J., Stimpson, C.D., Kim, Y.D., Raghanti, M.A., Lewandowski, A.H., Hof, P.R., Gómez-Robles, A., Krienen, F.M. & Sherwood, C.C. Gradients in cytoarchitectural landscapes of the isocortex: Diprotodont marsupials in comparison to eutherian mammals. *Journal of Comparative Neurology* **525**, 1811-1826 (2017).
5. Cahalane, D.J., Charvet, C.J. & Finlay, B.L. Modeling local and cross-species neuron number variations in the cerebral cortex as arising from a common mechanism. *Proceedings of the National Academy of Sciences* **111**, 17642-17647 (2014).
6. Charvet, C.J. & Finlay, B.L. Evo-Devo and the Primate Isocortex: The Central Organizing Role of Intrinsic Gradients of Neurogenesis. *Brain, Behavior and Evolution* **84**, 81-92 (2014).
7. Choi, E.Y., Yeo, B.T. & Buckner, R.L. The organization of the human striatum estimated by intrinsic functional connectivity. *Journal of neurophysiology* **108**, 2242-2263 (2012).
8. Glasser, M.F., Coalson, T.S., Bijsterbosch, J.D., Harrison, S.J., Harms, M.P., Anticevic, A., Van Essen, D.C. & Smith, S.M. Using temporal ICA to selectively remove global noise while preserving global signal in functional MRI data. *NeuroImage* **181**, 692-717 (2018).
9. Glasser, M.F., Smith, S.M., Marcus, D.S., Andersson, J.L., Auerbach, E.J., Behrens, T.E., Coalson, T.S., Harms, M.P., Jenkinson, M., Moeller, S., Robinson, E.C., Sotiroopoulos, S.N., Xu, J., Yacoub, E., Ugurbil, K. & Van Essen, D.C. The Human Connectome Project's neuroimaging approach. *Nature neuroscience* **19**, 1175-1187 (2016).
10. Morel, A., Magnin, M. & Jeanmonod, D. Multiarchitectonic and stereotactic atlas of the human thalamus. *The Journal of comparative neurology* **387**, 588-630 (1997).
11. Amunts, K., Kedo, O., Kindler, M., Pieperhoff, P., Mohlberg, H., Shah, N.J., Habel, U., Schneider, F. & Zilles, K. Cytoarchitectonic mapping of the human amygdala, hippocampal region and entorhinal cortex: intersubject variability and probability maps. *Anatomy and embryology* **210**, 343-352 (2005).
12. Eickhoff, S.B., Stephan, K.E., Mohlberg, H., Grefkes, C., Fink, G.R., Amunts, K. & Zilles, K. A new SPM toolbox for combining probabilistic cytoarchitectonic maps and functional imaging data. *Neuroimage* **25**, 1325-1335 (2005).
13. Greicius, M.D., Krasnow, B., Reiss, A.L. & Menon, V. Functional connectivity in the resting brain: A network analysis of the default mode hypothesis. *Proceedings of the National Academy of Sciences* **100**, 253-258 (2003).
14. Vincent, J.L., Kahn, I., Snyder, A.Z., Raichle, M.E. & Buckner, R.L. Evidence for a frontoparietal control system revealed by intrinsic functional connectivity. *Journal of neurophysiology* **100**, 3328-3342 (2008).

15. Marquand, A.F., Haak, K.V. & Beckmann, C.F. Functional corticostriatal connection topographies predict goal directed behaviour in humans. *Nature human behaviour* **1**, 0146 (2017).
16. Haber, S.N., Fudge, J.L. & McFarland, N.R. Striatonigrostriatal pathways in primates form an ascending spiral from the shell to the dorsolateral striatum. *The Journal of neuroscience : the official journal of the Society for Neuroscience* **20**, 2369-2382 (2000).
17. Haber, S.N. & Knutson, B. The reward circuit: linking primate anatomy and human imaging. *Neuropsychopharmacology* **35**, 4-26 (2010).
18. Dosenbach, N.U., Fair, D.A., Miezin, F.M., Cohen, A.L., Wenger, K.K., Dosenbach, R.A., Fox, M.D., Snyder, A.Z., Vincent, J.L., Raichle, M.E., Schlaggar, B.L. & Petersen, S.E. Distinct brain networks for adaptive and stable task control in humans. *Proceedings of the National Academy of Sciences of the United States of America* **104**, 11073-11078 (2007).
19. Dosenbach, N.U.F., Visscher, K.M., Palmer, E.D., Miezin, F.M., Wenger, K.K., Kang, H.C., Burgund, E.D., Grimes, A.L., Schlaggar, B.L. & Petersen, S.E. A Core System for the Implementation of Task Sets. *Neuron* **50**, 799-812 (2006).
20. Gordon, E.M., Laumann, T.O., Adeyemo, B., Huckins, J.F., Kelley, W.M. & Petersen, S.E. Generation and Evaluation of a Cortical Area Parcellation from Resting-State Correlations. *Cerebral cortex (New York, N.Y. : 1991)* **26**, 288-303 (2016).
21. Barch, D.M., Burgess, G.C., Harms, M.P., Petersen, S.E., Schlaggar, B.L., Corbetta, M., Glasser, M.F., Curtiss, S., Dixit, S., Feldt, C., Nolan, D., Bryant, E., Hartley, T., Footer, O., Bjork, J.M., Poldrack, R., Smith, S., Johansen-Berg, H., Snyder, A.Z. & Van Essen, D.C. Function in the human connectome: task-fMRI and individual differences in behavior. *Neuroimage* **80**, 169-189 (2013).
22. Blondel, V.D., Guillaume, J.-L., Lambiotte, R. & Lefebvre, E. Fast unfolding of communities in large networks. *Journal of Statistical Mechanics: Theory and Experiment* **2008**, P10008 (2008).
23. Plachti, A., Eickhoff, S.B., Hoffstaedter, F., Patil, K.R., Laird, A.R., Fox, P.T., Amunts, K. & Genon, S. Multimodal Parcellations and Extensive Behavioral Profiling Tackling the Hippocampus Gradient. *Cerebral cortex (New York, N.Y. : 1991)* (2019).
24. Behrens, T.E., Johansen-Berg, H., Woolrich, M.W., Smith, S.M., Wheeler-Kingshott, C.A., Boulby, P.A., Barker, G.J., Sillery, E.L., Sheehan, K., Ciccarelli, O., Thompson, A.J., Brady, J.M. & Matthews, P.M. Non-invasive mapping of connections between human thalamus and cortex using diffusion imaging. *Nature neuroscience* **6**, 750-757 (2003).
25. Janssen, R.J., Jylänki, P., Kessels, R.P.C. & van Gerven, M.A.J. Probabilistic model-based functional parcellation reveals a robust, fine-grained subdivision of the striatum. *NeuroImage* **119**, 398-405 (2015).
26. Ji, J.L., Spronk, M., Kulkarni, K., Repovs, G., Anticevic, A. & Cole, M.W. Mapping the human brain's cortical-subcortical functional network organization. *NeuroImage* **185**, 35-57 (2019).
27. Fan, L., Li, H., Zhuo, J., Zhang, Y., Wang, J., Chen, L., Yang, Z., Chu, C., Xie, S., Laird, A.R., Fox, P.T., Eickhoff, S.B., Yu, C. & Jiang, T. The Human Brainnetome Atlas: A New Brain Atlas Based on Connectional Architecture. *Cerebral cortex (New York, N.Y. : 1991)* **26**, 3508-3526 (2016).